OPEN ACCESS



On the Dwarf Irregular Galaxy NGC 6822. I. Young, Intermediate, and Old Stellar Populations

Maria Tantalo^{1,2}, Massimo Dall'Ora³, Giuseppe Bono^{1,2}, Peter B. Stetson⁴, Michele Fabrizio^{2,5}, Ivan Ferraro², Mario Nonino⁶, Vittorio F. Braga^{2,5,7}, Ronaldo da Silva^{2,5}, Giuliana Fiorentino², Giacinto Iannicola², Massimo Marengo⁸, Matteo Monelli^{7,9}, Joseph P. Mullen⁸, Adriano Pietrinferni¹⁰, and Maurizio Salaris^{11,10} Dipartimento di Fisica, Università di Roma Tor Vergata, via della Ricerca Scientifica 1, I-00133 Roma, Italy; maria.tantalo@students.uniroma2.eu, maria.tantalo@inaf.it

² INAF—Osservatorio Astronomico di Roma, via Frascati 33, I-00078 Monte Porzio Catone, Italy

³ INAF—Osservatorio Astronomico di Capodimonte, Salita Moiariello 16, I-80131 Napoli, Italy

Herzberg Astronomy and Astrophysics, National Research Council, 5071 West Saanich Road, Victoria, BC V9E 2E7, Canada
 ⁵ Space Science Data Center, via del Politecnico snc, I-00133 Roma, Italy
 ⁶ INAF—Osservatorio Astronomico di Trieste, Via G.B. Tiepolo 11, I-34143 Trieste, Italy
 ⁷ Instituto de Astrofísica de Canarias, Calle Via Lactea s/n, E-38205 La Laguna, Tenerife, Spain
 ⁸ Department of Physics and Astronomy, Iowa State University, Ames, IA 50011, USA
 ⁹ Departamento de Astrofísica, Universidad de La Laguna (ULL), E-38200, La Laguna, Tenerife, Spain
 ¹⁰ INAF—Osservatorio Astronomico dAbruzzo, via M. Maggini, s/n, I-64100, Teramo, Italy

 Astrophysics Research Institute, Liverpool John Moores University, 146 Brownlow Hill, Liverpool L3 5RF, UK
 Received 2022 April 1; revised 2022 May 23; accepted 2022 May 27; published 2022 July 14

Abstract

We present accurate and deep multiband (g, r, i) photometry of the Local Group dwarf irregular galaxy NGC 6822. The images were collected with wide-field cameras at 2 m/4 m (INT, CTIO, CFHT) and 8 m class telescopes (Subaru) covering a 2 deg² field of view across the center of the galaxy. We performed point-spread function photometry of \approx 7000 CCD images, and the final catalog includes more than 1 million objects. We developed a new approach to identify candidate field and galaxy stars and performed a new estimate of the galaxy center by using old stellar tracers, finding that it differs by 1'15 (R.A.) and 1'53 (decl.) from previous estimates. We also found that young (main sequence, red supergiants), intermediate (red clump, asymptotic giant branch (AGB)), and old (red giant branch) stars display different radial distributions. The old stellar population is spherically distributed and extends to radial distances larger than previously estimated (\sim 1°). The young population shows a well-defined bar and a disk-like distribution, as suggested by radio measurements, that is off-center compared with the old population. We discuss pros and cons of the different diagnostics adopted to identify AGB stars and develop new ones based on optical–near-IR–mid-IR color–color diagrams to characterize oxygen- and carbon-rich stars. We found a mean population ratio between carbon and M-type (C/M) stars of 0.67 \pm 0.08 (optical/near-IR/mid-IR), and we used the observed C/M ratio with empirical C/M–metallicity relations to estimate a mean iron abundance of [Fe/H] \sim -1.25 (σ = 0.04 dex), which agrees quite well with literature estimates.

Unified Astronomy Thesaurus concepts: Dwarf irregular galaxies (417); Stellar photometry (1620); Stellar populations (1622); Asymptotic giant branch stars (2100); Metallicity (1031)

1. Introduction

Stellar systems hosting stellar populations ranging from very young (a few Myr) main-sequence stars to old ($t > 10\,\mathrm{Gyr}$) low-mass stars are rare in the Local Group (LG). The most prominent systems, except for the three large LG galaxies (Milky Way (MW), M31, M33), are the Magellanic Clouds (MCs). However, we still lack firm theoretical and empirical constraints of their mutual dynamical interaction and of their interaction with the MW. This means that the star formation episodes and their chemical enrichment histories might have been either affected or driven by the environment. The next three stellar systems sharing similar metallicity distributions and hosting Wolf-Rayet stars are the three LG dwarf irregulars IC 10, IC 1613, and NGC 6822 (Neugent & Massey 2019). These three systems are considered unique analogs of star-forming galaxies observed at high redshift and populating the

Original content from this work may be used under the terms of the Creative Commons Attribution 4.0 licence. Any further distribution of this work must maintain attribution to the author(s) and the title of the work, journal citation and DOI.

universe at the peak of cosmic star formation history (Stott et al. 2013; Du et al. 2020).

NGC 6822 brings forward several key properties that make this stellar system particularly interesting (key positional, structural, and photometric properties are listed in Table 1). (a) The position on the sky $(\alpha_{1950} = 19^{\text{h}}42^{\text{m}}04^{\text{s}}.2, \ \delta_{1950} = -14^{\circ}56'24'';$ Gottesman & Weliachew 1977) is such that it can be observed from both the Northern Hemisphere and the Southern Hemisphere. (b) The true distance modulus based on the tip of the red giant branch (TRGB) is $\mu = 23.54 \pm 0.05$ mag (Lee et al. 1993; Fusco et al. 2012), which agrees quite well with similar estimates based on different standard candles (classical Cepheids, Gieren et al. 2006; Madore et al. 2009; Feast et al. 2012; Rich et al. 2014; Mira variables, Whitelock et al. 2013; carbon stars, Parada et al. 2021). The reddening shows a clumpy distribution, and the current estimates show a broad variety when moving from the region close to the galaxy center $(E(B - V) \sim 0.45 \text{ mag})$ to the outermost ($E(B-V) \sim 0.25$ mag) regions (Massey et al. 1995; Gallart et al. 1996; Gieren et al. 2006; Cannon et al. 2006; Fusco et al. 2012). This means that NGC 6822 is a factor of two closer in distance and less affected by differential reddening when

 Table 1

 Positional, Structural, and Photometric Properties of NGC 6822

Parameter		Reference
$\alpha \text{ (J1950)}^{\text{a}}$	19 ^h 42 ^m 04 ^s .2	[1]
$\delta (J1950)^a$	-14°56′24″	[1]
$R_{\rm half} (arcmin)^{\rm b}$	$16.13 \pm 0.5^{\mathrm{m}}$	[2]
$r_t (arcmin)^c$	40 ± 10	[3]
$\theta (\deg)^d$	62	[2]
ϵ e	0.35	[2]
$V (\text{mag})^{\mathbf{f}}$	8.1 ± 0.2	[4]
$M_V (\text{mag})^{\mathbf{g}}$	-15.2 ± 0.2	[5]
$(m-M)_0 (\text{mag})^{\text{h}}$	23.38 ± 0.04	[6]
$E(B-V) \text{ (mag)}^{i}$	0.35 ± 0.04	[6]
[Fe/H] ^j	-1.05 ± 0.01	[7]
$[Z]^{k}$	-0.52 ± 0.21	[8]
$[O/H]^{I}$	-0.55	[9]

Notes.

- ^a Galaxy center based on neutral hydrogen radio measurements.
- ^b Half-light radius.
- ^c Truncation radius.
- d Position angle.
- ^e Eccentricity.
- f Apparent visual magnitude.
- ^g Absolute visual magnitude.
- h True distance modulus.
- ⁱ Color excess.
- Mean iron abundance of the old population.
- k Mean metallicity of the young population.
- Mean oxygen abundance of H II regions.

References. [1] Gottesman & Weliachew (1977); [2] Zhang et al. 2021; [3] Hodge et al. (1991); [4] Dale et al. (2007); [5] McConnachie (2012) [6] Rich et al. (2014); [7] Kirby et al. (2013); [8] Patrick et al. (2015); [9] Lee et al. (2006).

compared with IC 10. (c) The metallicity distribution based on medium-resolution spectra shows a well-defined peak located at $[Fe/H] = -1.05 \pm 0.01$ and a standard deviation of $\sigma = 0.49$ dex (Kirby et al. 2013). This measurement suggests that its mean chemical composition is, within the errors, quite similar to IC 1613 ($[Fe/H] = -1.19 \pm 0.01$, $\sigma = 0.37$ dex). However, this iron abundance refers to the old stellar population in NGC 6822. Metallicity measurements for the young stellar population have also been widely investigated. From the spectra of two A-type supergiants Venn et al. (2001) found a mean iron abundance of $[Fe/H] = -0.49 \pm 0.22$, while Lee et al. (2006) obtained a mean oxygen abundance of [O/H] = -0.55 from optical spectra of five H II regions. More recently, Patrick et al. (2015) found a mean metallicity of $[Z] = -0.52 \pm 0.21$ by using medium-resolution near-IR (NIR) spectra of 11 red supergiants (RSGs).

The difference in metallicity between old and young stellar populations and the possible presence of a metallicity gradient in the innermost galaxy regions were explained by Patrick et al. (2015) using a closed-box chemical evolution model. This model is based on plane physical arguments and takes account of the increase in the mean metallicity when moving from old to young stellar populations. However, NGC 6822 has a complex morphology, and larger samples of old and young stellar tracers and more detailed chemical evolution models are required to constrain its chemical enrichment history. The measurements of the α -element abundances are quite limited and restricted to two globular clusters (GCs) of NGC 6822: Larsen et al. (2018) have

provided abundances for NGC 6822 SC6 ([Mg/Fe] = +0.295with rms = 0.240, [Ca/Fe] = +0.228 with rms = 0.170, [Ti/Fe] = +0.290 with rms = 0.091) and for NGC 6822 SC7 ([Mg/Fe] = -0.180 with rms = 0.208, [Ca/Fe] = +0.042 withrms = 0.141, [Ti/Fe] = +0.013 with rms = 0.128). They found measurements consistent with those of nearby dwarf galaxies and also the first evidence of the knee in the $[\alpha/Fe]$ versus [Fe/H]relation. (d) NGC 6822, thanks to its modest distance, has been the crossroad of multiband investigations ranging from the optical to the NIR and to the mid-infrared (MIR) of young stellar objects (YSOs) and asymptotic giant branch (AGB) stars (Letarte et al. 2002, hereafter L02; Kinson et al. 2021; Parada et al. 2021). These investigations have been soundly complemented by low-(Kacharov et al. 2012, hereafter K12) and medium-resolution spectroscopy (Sibbons et al. 2012, 2015, hereafter S12, S15). (e) This galaxy has also aroused great interest concerning the search, the identification, and the characterization of variable stars. Optical time series data covering a time interval of months were collected by Pietrzyński et al. (2004). They identified 116 classical Cepheids, together with sizable samples of long-period variables (LPVs) and eclipsing binaries (Mennickent et al. 2006). More recently, a detailed census of LPVs and candidate LPVs was also provided by collecting NIR time series: Battinelli & Demers (2011), using the wide-field imager CPAPIR at the Cerro Tololo Inter-American Observatory (CTIO), have found 64 LPVs; Whitelock et al. (2013), using the IRSF at SIRIUS, have provided a list of 157 LPV stars. These investigations were soundly complemented with fainter time series data collected with FORS2 at VLT by Clementini et al. (2003) and by Baldacci et al. (2005). They identified large samples of LPVs, eclipsing binaries, Chepheids, and, for the first time, a sample of 41 candidate RR Lyrae (RRL) variables. (f) NGC 6822 is one of the few nearby dwarf galaxies to host a spatially extended system of GCs. To date, eight GCs belonging to the galaxy have already been identified (Hubble 1925; Hwang et al. 2011; Huxor et al. 2013), and their structural properties are fundamental to probe the galaxy assembly process. (g) NGC 6822 was one of the very first dwarf galaxies to be discovered, and for this reason it held an important role in defining the scale of cosmic distances. The first distance estimate of NGC 6822 was determined by Shapley (1923) and subsequently redefined by Hubble (1925). Its stellar content was a stepping stone for the concept of stellar populations and for the cosmic distance scale. (h) The mean metal-intermediate chemical composition and the identification of solid young (classical Cepheids), intermediate-age (LPVs), and old (RRLs) stellar tracers and their apparent isolation make this stellar system a very interesting laboratory for stellar pulsation and evolution and to investigate galactic evolution.

The photometric investigations available in the literature and focused on NGC 6822 have moved along two different paths. (a) *Small and deep*: Detailed photometric investigations have been performed by using deep and accurate photometric images of several HST/ACS fields located across the disk of the galaxy by Cannon et al. (2012) and by Fusco et al. (2012, 2014). The color–magnitude diagrams (CMDs) approached the turnoff of the old stellar populations, and the star formation histories based on these data provided detailed information of the radial distribution of young, intermediate, and old stellar populations. The same outcome applies to the ground-based optical photometry collected with 8 m telescopes and to the space-based MIR photometry collected with Spitzer because the field of view (FOV) of the adopted detectors was quite

^m The $R_{\rm half}$ value was obtained by using the relation $R_{\rm half} = 1.68 r_0$ (Zhang et al. 2021) under the assumption of an exponential density profile and with the scale length provided by Zhang et al. (2021), $r_0 = 9.6 \pm 0.3$.

limited and of the order of tens of arcmin squared. (b) *Large and shallow*: Several optical and NIR ground-based photometric investigations have also been performed by using widefield imagers at the 2–4 m class telescopes. This means that they mainly focused either on young (YSOs, massive mainsequence stars) or on intermediate-age (AGB) stellar tracers over the entire body of the galaxy.

This is the first paper of a series aimed at studying the stellar content of NGC 6822 by taking advantage of optical photometry collected with wide-field imagers available at the 4–8 m class telescopes. In this investigation we will focus our attention on the photometric properties and the structure parameters of the galaxy and discuss in detail the radial distribution of a broad range of stellar populations and the C/M ratio derived from the AGB star count.

2. Observations and Data Reduction

Our photometric catalog was obtained by using a sizable sample of multiband (g, r, i) images collected with Hyper Suprime-Cam (HSC) at Maunakea Subaru Telescope. The individual images were collected by rotating the camera by 45° in consecutive exposures to fill the gaps among CCDs and to overcome difficulties with bright saturated stars (blooming) and with artifacts on individual CCDs. The HSC has an FOV of 1°.5 in diameter, with a 0".17 pixel⁻¹ scale. These images include both deep and shallow exposures, acquired during three different nights: 2014 September 29 (r band), 2015 October 7, and 2016 June 7 (g and i band). The shallow exposures include four r-, one g-, and three i-band images, each with an exposure time of 30 s. The deep exposures include 14 r-, 60 g-, and 24 i-band images, with exposure times of 300 s for the r band and 240 s for both the g and i bands. The HSC is equipped with 104 CCDs, but the current photometric catalog does not include a few of the most external ones. This data set was complemented with multiband images collected with the wide-field imager MegaPrime available at the Canada-France-Hawaii Telescope (CFHT), with the Dark Energy Camera (DECam) on the Blanco telescope at CTIO, and with the Wide Field Camera (WFC) mounted on the Isaac Newton Telescope (INT) at La Palma. Actually, these three optical data sets were included to improve the absolute photometric calibration and the sampling of bright stars. The images from the CFHT were acquired between 2004 May 26 and June 25 and include three r-, three g-, and seven i-band images, and their exposure times range from 15 to 150 s. The MegaPrime has an FOV of $1 \times 1 \text{ deg}^2$ with a 0".19 pixel⁻¹ scale. The data acquired at the Blanco telescope include eight r-, eight g-, and eight i-band images collected over three nights (2016 May 28, July 4, and July 5), and their exposure times range from 30 to 80 s. The DECam has an FOV of 2.2 deg² in diameter with a 0".27 pixel⁻¹ scale. Finally, the images from the INT include six gband exposures collected during two nights on 2003 May 1 and 3 and have an exposure time of about 600 s. The WFC has a $34' \times 34'$ FOV with a 0."33 pixel⁻¹ scale. All in all, the current data set covers 2 deg² across the center of the galaxy and a time interval of 13 yr. The seeing distribution of individual CCD images included in the data set is plotted in Figure 1; it suggests that 25% of the images were collected with a seeing better than 0."6 and 60% with a seeing better than 1". The log of the observing runs is summarized in Table 2. Figure 2 shows the sky coverage of the different data sets used in this study. The left panel displays the coverage of the HSC (shallow and deep),

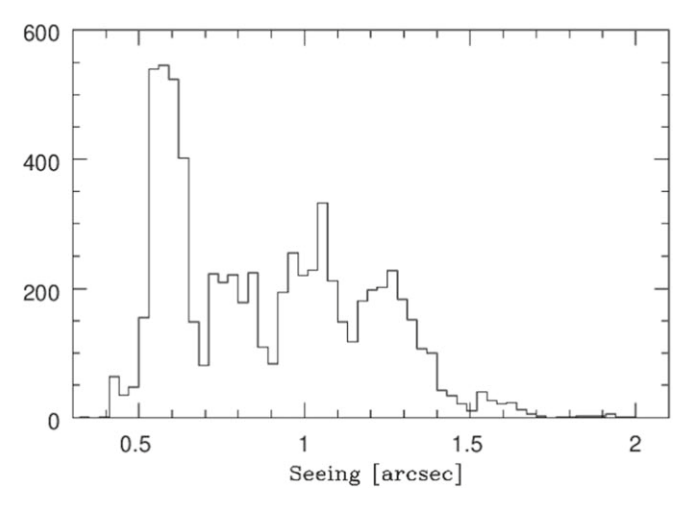


Figure 1. Seeing distribution of individual CCD images included in the data set.

the MegaPrime, the DECam, and the WFC g-, r-, and i-band exposures. The right panel shows the sky coverage of the IR catalogs available in the literature for NGC 6822:12 (i) NIR catalog (black circles; (S12)) covering an area of 1.8 deg² across the galaxy center and acquired at the 3.8 m United Kingdom Infrared Telescope (UKIRT) with the Wide Field CAMera (WFCAM; 0."4 pixel⁻¹ scale) as part of the UKIRT Infrared Deep Sky Survey (UKIDSS; Warren et al. 2007); (ii) MIR photometry (red circles; Khan et al. 2015) covering the innermost (5.2 \times 5.2 squared) central regions and collected from the mosaics of the SIRTF Nearby Galaxies Survey (SINGS; Kennicutt et al. 2003) by using the Infrared Array Camera (IRAC; 1"2 pixel⁻¹ scale) on board Spitzer; (iii) MIR photometry (magenta circles) obtained with the Wide-field Infrared Survey Explorer (WISE; Wright et al. 2010), covering an area of $3^{\circ} \times 3^{\circ}$ centered on the galaxy. The data have been extracted from the CatWISE2020 catalog (Marocco et al. 2021) at 3.4 and 4.6 μ m (W1 and W2 bands, respectively) and from the AllWISE release of the WISE Source Catalog (Cutri et al. 2013) at 12 μ m (W3 band). The reasons why we decided to use the NIR and MIR catalogs will become clearer in the following sections.

The data reduction was mainly performed with the DAO-PHOT-ALLSTAR-ALLFRAME packages (Stetson 1987, 1994). For the HSC images we adopted the following procedure: as a first step, the point-spread functions (PSFs) of the stars on individual images have been computed through a custom automatic pipeline, based on a suite of DAOPHOT/ALLSTAR SExtractor (Bertin & Arnouts 1996) Python FORTRAN routines, which discards outliers, extended sources, and blends and performs the WCS alignment. Subsequently, the ALLFRAME routine was used to improve the PSF photometry on the different sets of CCDs covering the same FOV area. The instrumental magnitudes thus obtained were calibrated to the Pan-STARRS g, r, i standard system by using a list of 41,720 stars from the Pan-STARRS catalog. The derived transformation equations for each image include first- and second-order color terms, zero-points, and linear positional terms (X and Y) and have standard deviations of 0.015, 0.012, and 0.010 mag in the g, r, and i bands, respectively.

¹² The NIR (S12) and MIR (Khan et al. 2015) catalogs are available on the VizieR database at https://vizier.u-strasbg.fr/viz-bin/VizieR.

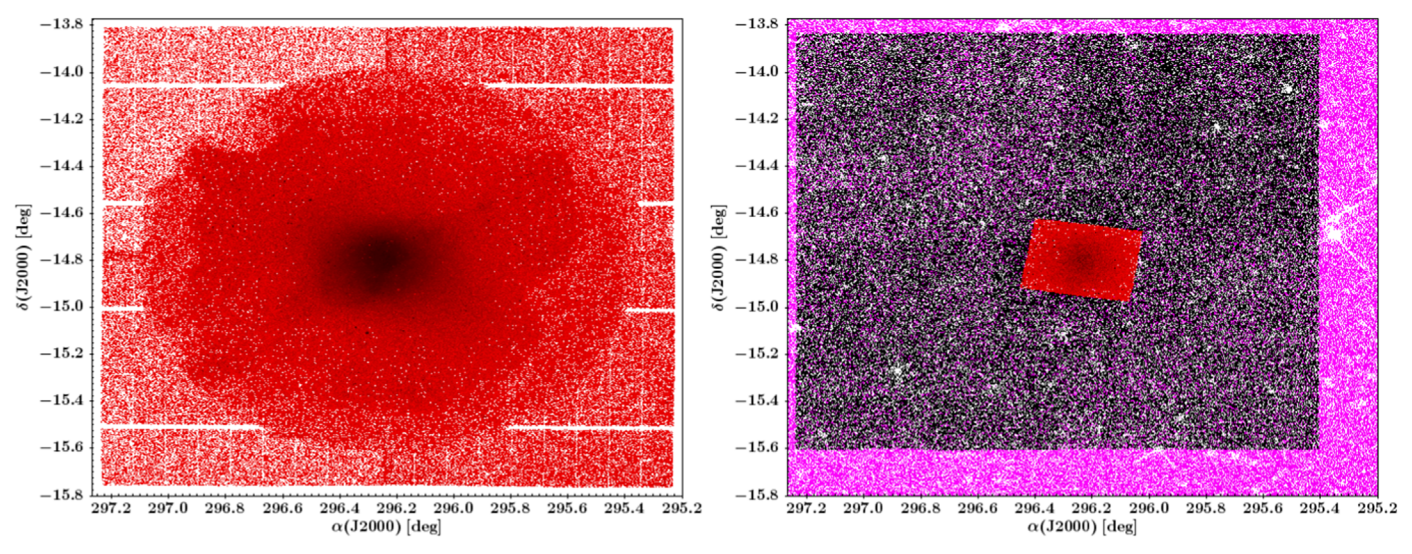


Figure 2. Left: sky coverage of the HSC (shallow and deep), MegaPrime, DECam, and WFC g, r, and i images. Right: same as the left panel, but for the WISE (magenta circles), UKIRT (black circles), and Spitzer (red circles) data sets.

Table 2
Summary of the Observing Runs for NGC 6822

Run Name	Dates	Telescope	Camera	N_r	N_g	N_i	Multiplex
suba29	2014 Sep 29	Subaru 8.2 m	Hyper Suprime-Cam	18			× 104
suba29	2015 Oct 7	Subaru 8.2 m	Hyper Suprime-Cam		25	12	× 104
suba29	2016 Jun 7	Subaru 8.2 m	Hyper Suprime-Cam		36	15	× 104
mp6822	2004 May 26 Jun 25	CFHT 3.6 m	MegaPrime	3	3	7	× 36
dec1605	2016 May 28	CTIO 4 m	DECam	4	4	4	× 34
dec1607	2016 Jul 4 5	CTIO 4 m	DECam	4	4	4	× 34
int0305	2003 May 1 3	INT 2.5 m	Wide Field Camera		6		\times 4

Note. The most external HSC CCDs have not been used to obtain our photometric catalog.

The final combined and photometrically calibrated catalog contains more than 1 million objects, and the limiting magnitudes range from 14 to 25.8 mag in the g band (the deepest), from 13.7 to 25.5 mag in the r band, and from 13 to 24.9 mag in the i band (the shallowest), thus providing the widest and most homogeneous photometric data set ever collected for a nearby dIrr, except for the MCs. The photometric errors typically range from 0.003 up to 0.01 mag for g, r, $i \le 20$ mag; range from 0.01 up to 0.02 mag for 20 mag $\langle g, r, i \leq 22 \text{ mag};$ and increase quite steeply from 0.02 up to 0.09 for g, r, i > 22 mag. The r, g-i CMD resulting from the entire optical data set is plotted in Figure 3, together with the error bars showing the intrinsic photometric errors both in magnitude and in color, for which they were summed in quadrature. The CMD shows some clear features of the NGC 6822 galaxy, such as the young main sequence (YMS) at $g - i \sim -0.2$ to 0 mag and the red giant branch (RGB) ranging over about 3.5 mag in magnitudes and 1.2 mag in color, but also a considerable number of foreground and background field stars; indeed, the two sequences of G-type stars at $g - i \sim$ 1 mag and M-type stars at $g-i \sim 2-3$ mag are particularly prominent.

3. Identification of Candidate Field and Galaxy Stars

The separation between candidate field and galaxy stars is one of the fundamental issues concerning the analysis of stellar populations in nearby stellar systems. Stellar systems located at low Galactic latitudes are severely affected by field contamination; therefore, star counts and the comparison between theory and observations in both optical and NIR CMDs are hampered by foreground and background Galactic stars. The problem becomes even more severe for gas-rich stellar systems because they are typically affected by differential reddening. NGC 6822 is affected by the quoted limitations, and to overcome these difficulties, special attention was paid to the separation between field and galaxy stars.

The approach we devised differs from the approach we have already adopted for ω Cen (Calamida et al. 2020) and nearby dwarf galaxies Carina (Bono et al. 2010b) and Sculptor (Martínez-Vázquez et al. 2016). NGC 6822 includes young, intermediate, and old stellar tracers; therefore, we developed a new method based on 3D color–color–magnitude diagrams (CCMDs). The initial step relies on the separation between the most relevant evolutionary features of candidate field and galaxy stars. To accomplish this goal, we selected two different regions located well outside the central regions of the galaxy (see yellow circles plotted in Figure 4(a)). The reasons for this selection are twofold:

 These regions are located outside the disk/bar and beyond the core radius. This means that they are less affected by crowding; therefore, their photometry is deeper and more accurate. Moreover, these regions are

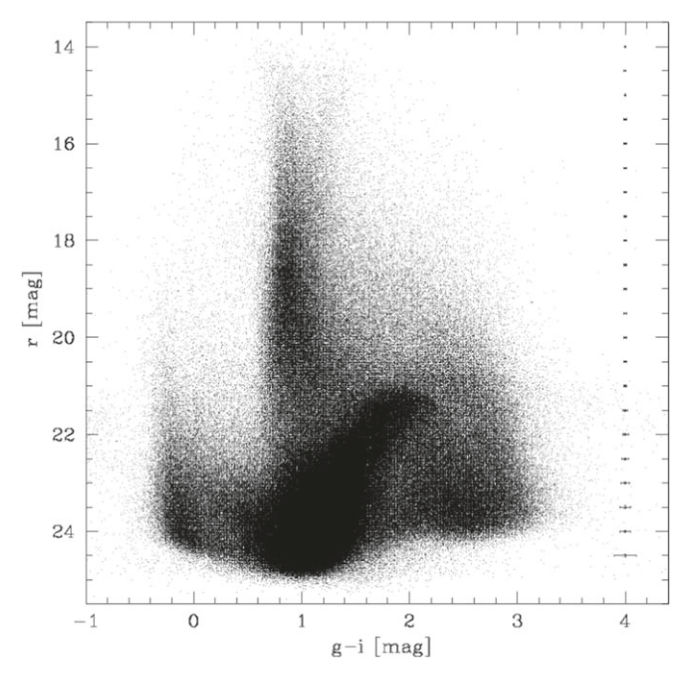


Figure 3. r, g-i CMD based on the entire optical data set. The error bars plotted on the right side of the CMD (g-i \sim 4 mag) display the intrinsic errors both in magnitude and in color (summed in quadrature).

- also less affected by differential reddening, and the evolutionary sequences are intrinsically narrower.
- 2. Star counts of both field and galaxy stars almost balance at these radial distances. This means a proper identification of the key evolutionary features. Indeed, at larger radial distances the CMD is dominated by field stars, whereas at smaller radial distances it is dominated by galaxy stars. Note that the sharp decrease in the stellar density of the most external regions is a consequence of the fact that these regions were only covered with shallow exposure times. Therefore, their limiting magnitude is 2/3 mag shallower than for the internal regions.

Figure 4(b) shows the 3D CCMD, g - r, r - i, r. We performed a preliminary identification of both candidate field stars, plotted with orange/red circles, and candidate galaxy stars, plotted on top with green circles. The different sequences were identified by using different view angles that help in the identification of both field and galaxy sequences. Moreover, to properly identify candidate galaxy stars, we also used different sets of stellar isochrones transformed into the Pan-STARRS photometric system from the BASTI database¹³ covering a broad range in stellar ages and chemical compositions (see discussion in Section 5.1). To make clearer the adopted procedure, Figure 4(c) shows the same stars in the CCMD, but the view is from the top of the Z-axis (r mag). Data plotted in these CCMDs allow us to properly identify candidate field stars, namely, the sequence of G-type stars located at $g-r \sim$ 0.4–0.8 mag and the more relevant sequence of M-type stars located at $g - r \sim 1.2$ –1.5 mag (Castellani et al. 2002; Girardi et al. 2012; Robin et al. 2014). After a number of tests and trials in which we took into account the luminosity and the color function, we also performed a preliminary identification of galactic RGB and early AGB sequences (green circles). To further highlight the difficulties in disentangling galaxy and field sequences, Figure 4(d) shows the same stars, but plotted in the g - r, r - i color-color diagram (CCD).

Note that candidate galaxy and field stars overlap over the entire color ranges. A glance at the data plotted in this CCD clearly shows that along the line of sight and at the quoted radial distances field stars outnumber candidate galaxy stars. Selections only based on colors will include a significant fraction of candidate field stars among candidate galaxy stars and vice versa. As a final validation of the selection criteria adopted to identify candidate field and galaxy stars, we also investigated their radial distributions. Figure 5 shows the radial distribution of the stars marked with yellow circles in Figure 4(a). We estimated the surface density of candidate field (red line) and galaxy (green line) stars in concentric annuli of equal area and plotted them as a function of the radial distance. The radial distributions were also smoothed by assuming a Gaussian kernel with unitary weight. Data plotted in this figure show that candidate field stars have, within the errors, a flat distribution over the entire area, while the candidate galaxy stars display, as expected, a steady decrease when moving from the innermost to the outermost galaxy regions.

Subsequently, we removed the sequence of candidate galaxy stars and were left with the CCMD shown in Figure 4(e). Data plotted in this figure show that the subtraction of candidate galaxy stars caused an oversubtraction of field stars in the region with colors ranging from $g - r \sim 0.0$ mag to $g - r \sim 1.5$ mag and from $r - i \sim 0.7$ mag to $r - i \sim 1.1$ mag, and with rmagnitudes ranging from $r \sim 23$ to ~ 18.5 mag. To overcome this problem, we split the same CCMD region of the candidate galaxy stars (see green circles in Figure 4(b)) into roughly two dozen contiguous slabs. We randomly extracted in each slab of candidate galaxy stars a number of stars that allowed us to have in each slab of candidate field stars a number of stars similar (within Poisson uncertainties) to the regions of the CCMD located at the edges of the gap caused by the subtraction of candidate galaxy stars. The outcome of the random extraction of possible field stars among candidate galaxy stars is displayed in Figure 4(f), in which the gap is no longer present. The new catalog of candidate field stars plotted in Figure 4(f) was statistically subtracted to the entire photometric catalog (yellow plus blue circles plotted in Figure 4(a)). The main outcomes of this process were two new subsamples of candidate field and galaxy stars. The latter subsample was used to improve the selection criteria adopted to separate field and galaxy stars (yellow circles in Figure 4(a)), and following once again the same steps discussed at the beginning of this section, we ended up with a final catalog of candidate galaxy stars including more than 550,000 stars with at least one measurement in two different photometric bands.

The final outcome is shown in Figure 6. The top panel displays the r, g-r CMDs for the whole photometric catalog (left), stars that are candidates to belong to NGC 6822 (middle), and field stars (right); the bottom panel is the same as the top panel, but for i, g-i CMDs. For the sake of clearness, we decided to plot one object over 10 selected from each catalog. Note that when field stars were removed, some well-defined evolutionary phases could be easily recognized: YMS stars (16 mag $\leqslant i \leqslant 24.5$ mag, $g-i \sim 0$ mag), RSGs (16 mag $\leqslant i \leqslant 20.5$ mag, 1.4 mag $\leqslant g-i \leqslant 2$ mag), the TRGB $(i \sim 20.5)$ mag, $g-i \sim 2$ mag), and AGB stars (19.5 mag $\leqslant i \leqslant 20.5$ mag, 1.8 mag $\leqslant g-i \leqslant 3.8$ mag). The

¹³ The interested reader is referred to http://basti-iac.oa-abruzzo.inaf.it/index.html.

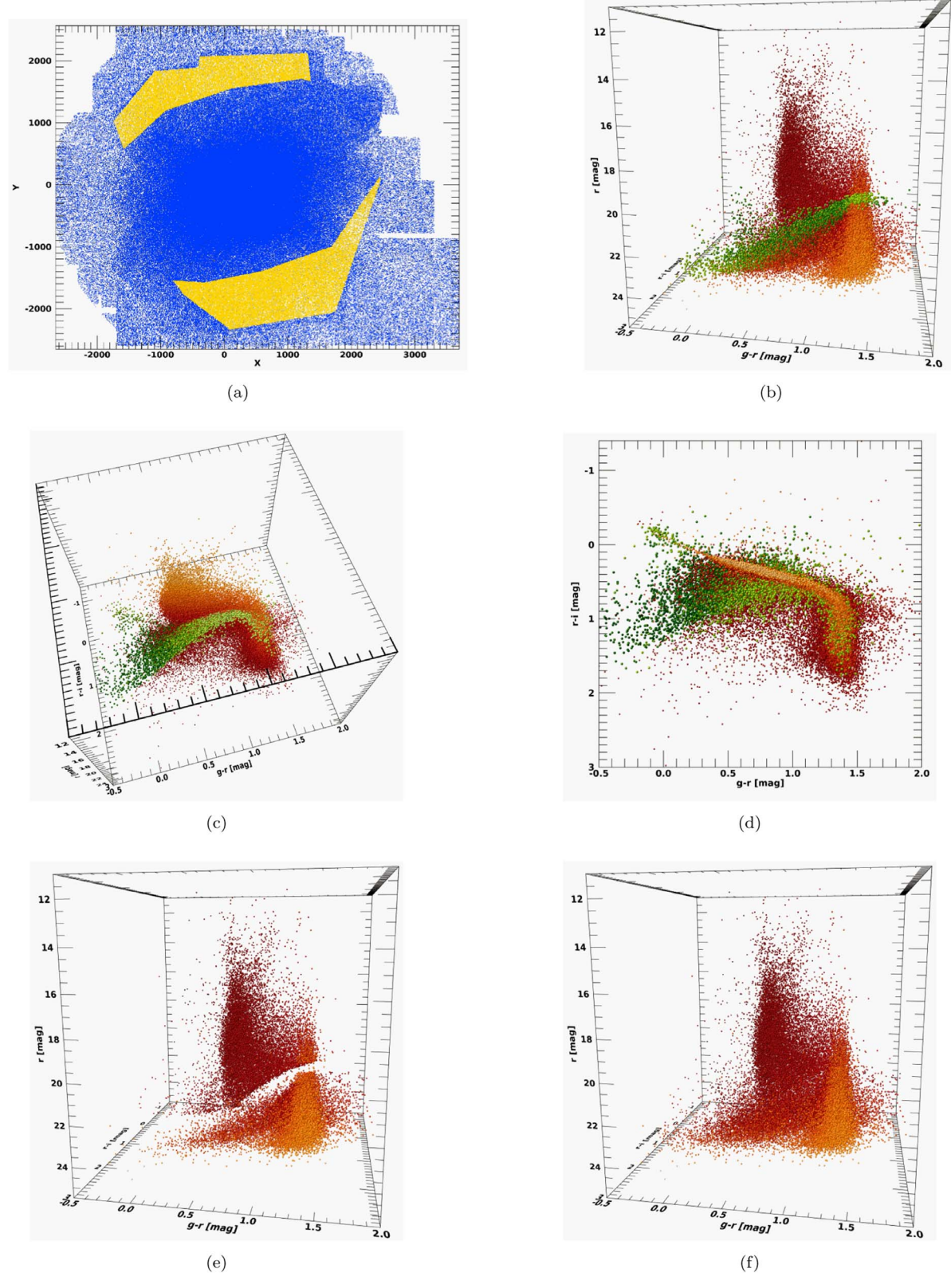


Figure 4. (a) Distribution on sky of the entire optical catalog (blue circles). The yellow circles display the regions adopted for selecting candidate galaxy stars. (b) The g-r, r-i, r CCMD. Green circles display candidate galaxy stars, while red circles display candidate field stars. (c) Same as panel (b), but with a different view angle. (d) Same as panel (b), but the view is from the top of the z-axis, i.e., projected onto the g-r, r-i CCD. (e) Same as panel (b), but we only plotted candidate field stars after the subtraction of candidate galaxy stars. (f) Same as panel (e), but the gap was filled by statistically subtracting stars from the sample of candidate galaxy stars. See text for more details.

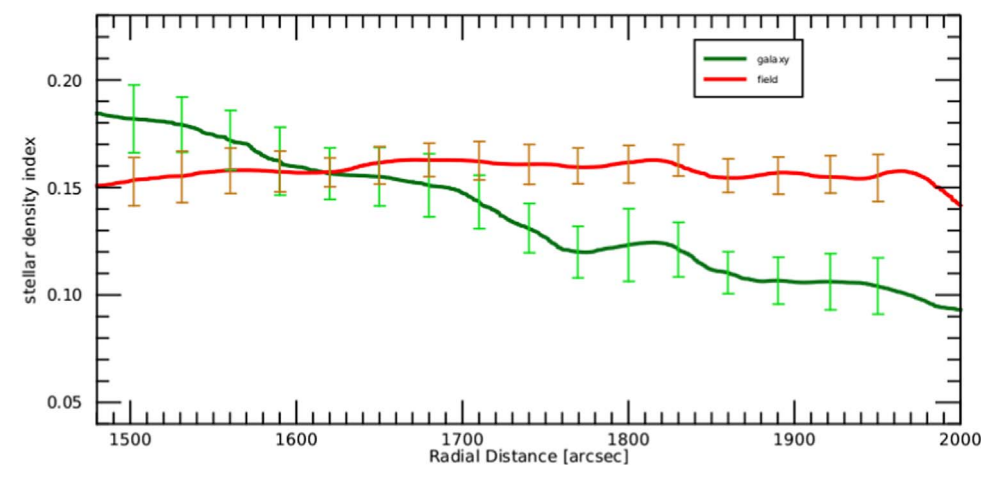


Figure 5. Surface density of candidate galaxy (green line) and field (red line) stars as a function of the radial distance for the stars marked with yellow circles in Figure 4(a). The radial distributions were smoothed by using a Gaussian kernel with unitary weight. The error bars display the standard deviation in the estimate of the surface density.

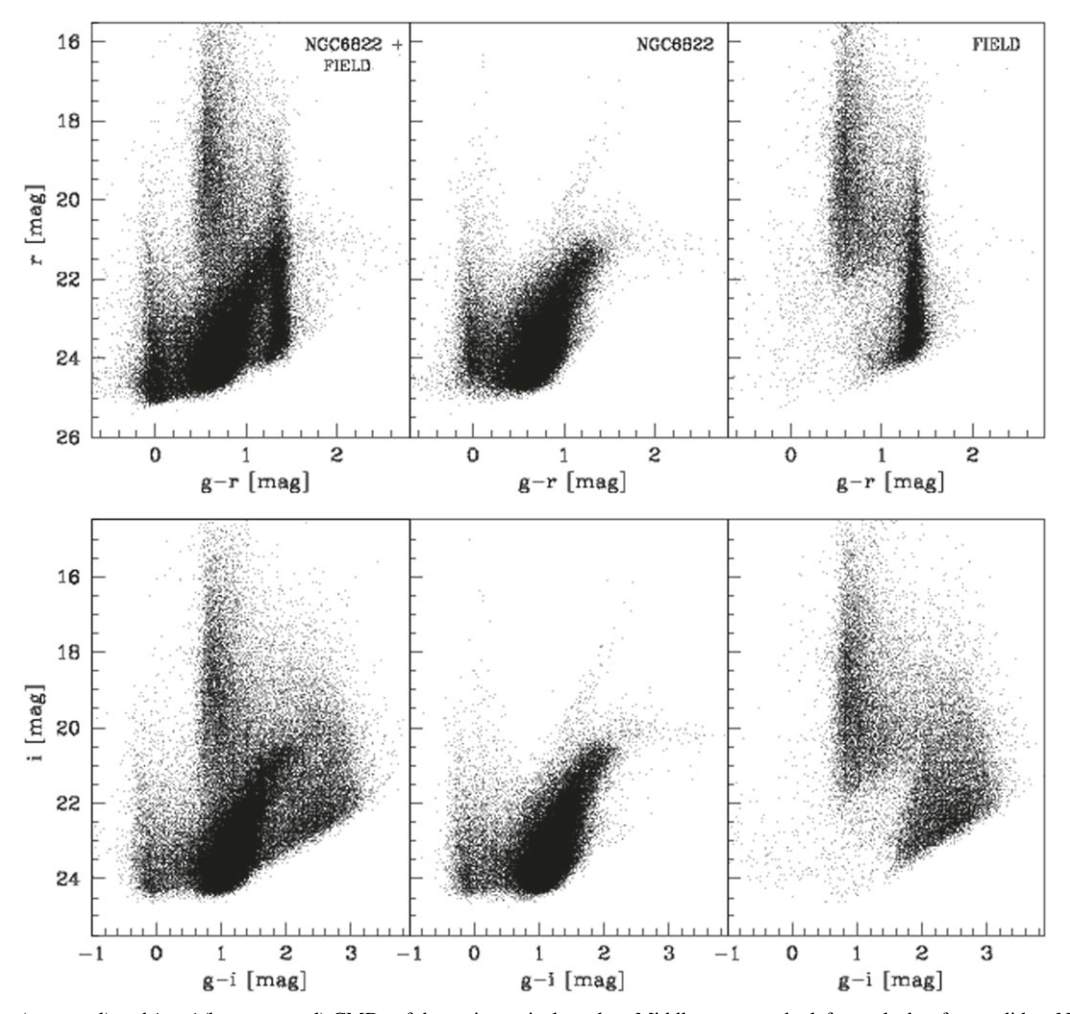


Figure 6. Left: r, g-r (top panel) and i, g-i (bottom panel) CMDs of the entire optical catalog. Middle: same as the left panels, but for candidate NGC 6822 stars. The data in this panel display several well-defined evolutionary phases: YMS stars (16 mag $\leq i \leq 24.5$ mag, $g-i \sim 0$ mag), RSGs (16 mag $\leq i \leq 20.5$ mag, 1.4 mag $\leq g-i \leq 2$ mag), the TRGB ($i \sim 20.5$ mag, $g-i \sim 2$ mag), and AGB stars (19.5 mag $\leq i \leq 20.5$ mag, 1.8 mag $\leq g-i \leq 3.8$ mag). Right: same as the left panels, but for candidate field stars. The CMDs shown in this figure only display 1 star out of every 10 in the global catalog.

candidate field stars plotted in the right panels show that the separation between field and galaxy stars can be improved; indeed, in the region between 19.5 mag $\leq i \leq$ 22.5 mag and 1.2 mag $\leq g - i \leq$ 1.8 mag, some galaxy stars could also be present.

The catalog of the candidate galaxy stars allows us to provide accurate estimates of the absolute magnitude of NGC 6822 in all of the investigated photometric bands. The mean apparent and absolute magnitudes are listed in Table 3,

Table 3

Total Apparent and Absolute Magnitudes for NGC 6822, the LMC, and the SMC

Band	Apparent (mag)	Absolute (mag)	Absolute ^a (mag)	Absolute for SMC ^c (mag)	Absolute for LMC ^c (mag)
g	8.43 ± 0.03	-15.03 ± 0.07		•••	
r	7.97 ± 0.03	-15.49 ± 0.07			
i	7.68 ± 0.04	-15.78 ± 0.08			
B	8.85 ± 0.05^{b}	$-14.61 \pm 0.08^{\circ}$	-14.62	-16.89 ± 0.06	-18.28 ± 0.05
V	8.93 ± 0.03^{b}	$-14.53 \pm 0.07^{\mathbf{b}}$	-15.09	-16.29 ± 0.06	-17.60 ± 0.05
J	7.91 ± 0.10	-15.55 ± 0.12	-17.35	-17.35 ± 0.06	-18.77 ± 0.05
H	7.29 ± 0.08	-16.17 ± 0.10	-17.83	-18.05 ± 0.06	-19.52 ± 0.05
K	7.10 ± 0.10	-16.36 ± 0.12	-18.29	-18.27 ± 0.06	-19.77 ± 0.05
W1	5.86 ± 0.09	-17.60 ± 0.11	-18.08	-18.24 ± 0.06	-19.60 ± 0.05
W2	5.76 ± 0.14	-17.70 ± 0.15	-18.25	-18.26 ± 0.06	-19.59 ± 0.05
W3	4.12 ± 0.33	-19.34 ± 0.34		-20.44 ± 0.06	-21.27 ± 0.05

Notes.

together with their uncertainties. We unreddened the apparent magnitudes of candidate galaxy stars by using the reddening map provided by Schlegel et al. (1998; E(B-V) = 0.24 mag) and the reddening law provided by Cardelli et al. (1989). Note that we decided to neglect the intrinsic reddening, since, according to the reddening map by Schlegel et al. (1998), the variation across the main body of the galaxy is $\Delta E(B-V) = 0.04$ mag. This means a minimal impact on the absolute magnitudes listed in Table 3. Then, the apparent unreddened magnitudes were transformed in fluxes, summed up, and transformed into magnitudes once again. Subsequently, the total apparent magnitudes were transformed into absolute magnitudes by adopting a true distance modulus of $\mu = 23.46 \pm 0.06$ mag, which is the mean value of the true distance moduli obtained by Fusco et al. (2012) using the TRGB and by Rich et al. (2014) using classical Cepheids. The g, r total, apparent, and mean absolute magnitudes were transformed into B, V apparent and absolute magnitudes by using the following linear transformations between Pan-STARRS and Johnson/Cousins photometric systems provided by Tonry et al. (2012): g - r = 0.213 + 0.587(B - g) and g-r=0.006+0.474(V-r). More detailed transformations based on the BVRI and on the g, r, i photometry available to our group will be provided in a forthcoming paper. Note that in order to estimate the total apparent magnitudes in W1 and W2 bands, we took into account the [3.6] and [4.5] measurements of candidate galaxy stars, covering the central regions and collected with IRAC@SPITZER, together with the W1 and W2 measurements covering the more external regions and collected by WISE. Actually, Cutri et al. (2013) found that the W1- and W2-band photometry is consistent with the IRAC@SPITZER magnitudes in the two equivalent bands [3.6] and [4.5], respectively, with only small differences, largely due to the small changes in bandpasses. This result has been confirmed in subsequent studies that found a negligible difference between the W1 and IRAC [3.6] bands and an offset of 0.028 mag between the W2 and IRAC [4.5] bands (Papovich et al. 2016).

This difference is reduced to less than 0.02 mag for late spectral type stars. Column (4) of the same table gives the absolute magnitudes available in the literature for NGC 6822. The B, W1, and W2 magnitudes are quite similar, within the errors, to the current estimates. On the contrary, the J, H, K absolute magnitudes are, on average, 2 mag fainter. The difference is mainly due to the fact that the J, H, K literature estimates are based on Two Micron All Sky Survey (2MASS) photometry that is shallower than UKIRT photometry, and typically they did not perform a separation between candidate field and galaxy stars. Columns (5) and (6) of the table list the total absolute magnitudes for the Large Magellanic Cloud (LMC) and the Small Magellanic Cloud (SMC) in the same photometric bands used for NGC 6822, with the exception of g, r, i. Apparent magnitudes for individual stars in the MCs are available in the Gaia eDR3 catalog, which provides measurements in the three Gaia photometric bands G, $G_{\rm BP}$, $G_{\rm RP}$; in the 2MASS NIR (J, H, K) bands; and in the AllWISE MIR (W1, W2, W3) bands (see Appendix B for more details). The individual apparent magnitudes were unreddened by using the reddening values provided by Joshi & Panchal (2019; E(B - $V_{LMC} = 0.091 \pm 0.050$ mag, $E(B - V)_{SMC} = 0.038 \pm 0.053$ mag), and then the total absolute magnitudes were estimated by using the true distance moduli from Pietrzyński et al. (2019; $\mu_{\rm LMC} = 18.477 \pm 0.004$ mag) and Graczyk et al. (2020; $\mu_{\rm SMC} = 18.977 \pm 0.016$ mag). Finally, the G, $G_{\rm BP}$, $G_{\rm RP}$ total absolute magnitudes were transformed into B, V absolute magnitudes by using the following color-color transformations between Gaia eDR3 and Johnson/Cousins photometric systems from Riello et al. (2021): G - V = -0.02704 + 0.01424 $(G_{\rm BP}-G_{\rm RP}) - 0.2156(G_{\rm BP}-G_{\rm RP})^2 + 0.01426(G_{\rm BP}-G_{\rm RP})^3$ and $G-V=-0.04749 - 0.0124(B-V) - 0.2901(B-V)^2 +$ $0.02008(B-V)^3$. The results show that NGC 6822 in all the listed photometric bands is fainter than the MCs. Moreover, the magnitudes in Table 3 indicate that NGC 6822 has optical-NIR colors similar to those of the MCs and optical-MIR colors that are systematically redder than MCs with a difference of the

^a Absolute magnitudes from the literature: *V*- and *B*-band magnitudes were obtained by using the total apparent magnitudes from Mateo (1998) and the same reddening and true distance modulus used for our estimates; total NIR/MIR magnitudes were estimated by using the global unreddened flux densities from Dale et al. (2007) and the same true distance modulus used for our estimates. Note that we neglected uncertainties on individual estimates, since they are very similar to the current ones.

^b V, B total apparent and absolute magnitudes were obtained by using the linear transformations between Pan-STARRS and Johnson/Cousins photometric systems from Tonry et al. (2012) (see text for more details).

c V, B total absolute magnitudes were obtained by using the color–color transformations between Gaia eDR3 and Johnson/Cousins photometric systems from Riello et al. (2021) (see text for more details). J, H, K in the 2MASS system and W1, W2, W3 in the AllWISE system were estimated from measurements in the Gaia eDR3 catalog.

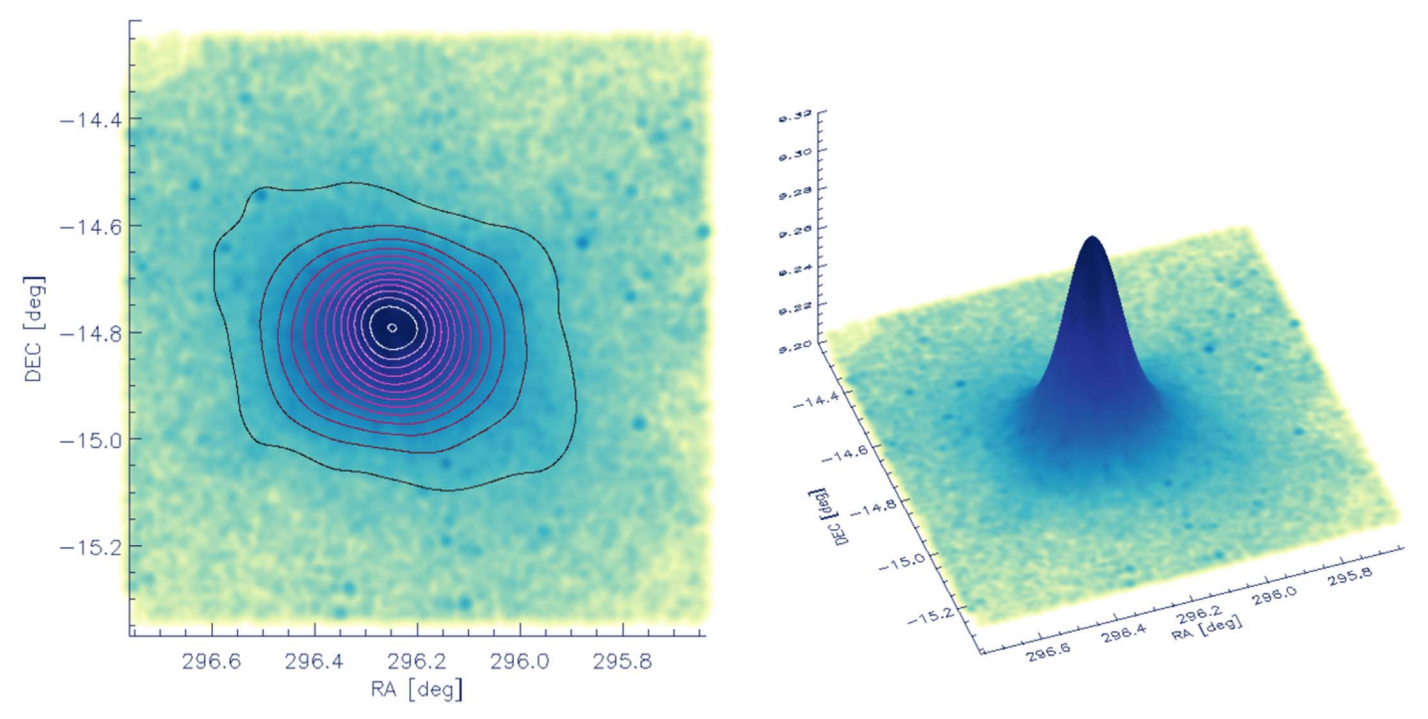


Figure 7. Left: radial distribution on the sky of the old stellar tracers (RGB+RHB), smoothed by assuming a Gaussian kernel with unitary weight. Overplotted are the isocontour levels. Right: 3D histogram (R.A., decl., N in arbitrary units), showing the symmetrical spherical distribution of the old stellar tracers, obtained by summing up the Gaussian of the entire sample of candidate NGC 6822 stars.

order of 1 mag. This difference is mainly caused by the large relative number of C-rich stars identified in NGC 6822.

In this context it is worth mentioning that the total apparent magnitudes in the three WISE photometric bands can be used as diagnostics to identify active galactic nuclei (AGNs) in dwarf galaxies. Indeed, Hainline et al. (2016) used the infrared WISE color-color (W1 – W2, W2 – W3) diagnostic diagram to separate the AGNs and the so-called "composite" galaxies, defined as stellar systems having contributions to their emission-line flux from both star formation and AGN activity (Baldwin et al. 1981; Kewley et al. 2001; Kauffmann et al. 2003). According to the current estimates, NGC 6822 has unreddened WISE colors of $W1 - W2 = 0.10 \,\text{mag}$ and W2 - W3 = 1.64 mag. This means that NGC 6822 is located along the blue tail of the "composite" galaxy sequence (see Figure 1 of Hainline et al. 2016). This evidence taken at face value indicates that in the selected sample of composite galaxies the AGB stars, and in particular C-rich stars, can contribute to their total flux, together with young stars (YMS, RSG) and possibly with AGN activity. The current findings suggest that MIR color space should be cautiously treated in the selection of AGNs in dwarf galaxies owing to the nontrivial contribution of young (Reines 2022) and, in particular, intermediate-age stellar populations.

4. A New Estimate of the Center of the Galaxy

The estimates of the center of NGC 6822 currently available date back to the 1970s and were performed by Gallouet et al. (1975, $\alpha_{1950} = 19^{\rm h}42^{\rm m}06^{\rm s}.4$, $\delta_{1950} = -14^{\circ}55'23''$) on the basis of optical photographic photometry and by Gottesman & Weliachew (1977, $\alpha_{1950} = 19^{\rm h}42^{\rm m}04^{\rm s}.2$, $\delta_{1950} = -14^{\circ}56'24''$) on the basis of radio measurements of neutral hydrogen across the core of NGC 6822. In Section 5.3 we plan to investigate in detail the radial distribution of young, intermediate, and old stellar tracers.

In order to provide accurate estimates of the different radial distributions, we performed a new and independent estimate of the center of the galaxy. To overcome possible systematics, we decided to follow two different approaches.

(i) 3D histogram.—To overcome possible differences among different stellar tracers, we removed from the global catalog of candidate galaxy stars the young (MS, RSGs) and the intermediate-age (AGB: C-rich, O-rich; red clump (RC) stars) stellar tracers. We only selected RGB stars and candidate red horizontal branch (HB) stars. The motivations for these selection criteria will become clearer in Section 5.3. The left panel of Figure 7 shows the radial distribution on the sky (R.A., decl.) of older stellar tracers, together with the isocontour levels. Note that the radial distribution was smoothed by assuming a unitary Gaussian kernel with sigma equal to the sum in quadrature of the errors on the position of the centroid. Finally, the Gaussians of individual candidate galactic stars were summed up and plotted on a 3D (R.A., decl., N [arbitrary units]) histogram, shown in the right panel of Figure 7.

Data plotted in this figure show that older stellar tracers attain a symmetrical spherical distribution over the entire body of the galaxy. We performed a Gaussian fit to the observed distribution, and the peak of the distribution—galaxy center—is located at: R.A.(J2000) = $19^{\rm h}44^{\rm m}58^{\rm s}.56$, decl.(J2000) = $-14^{\rm d}47^{\rm m}34^{\rm s}.8$. The new estimate is in fair agreement with the optical and radio values; indeed, it differs by 0.6 and 0/51 in R. A. and decl. from the estimate of Gallouet et al. (1975) and by 1/15 and 1/53 in R.A. and decl. from the estimate of Gottesman & Weliachew (1977).

(ii) Maximum likelihood.—To provide an independent estimate of the structural parameters of NGC 6822, we adopted the publicly available code provided by Martin et al. (2008). They developed a maximum likelihood algorithm to derive the structural parameters for a number of MW satellites. They validated the algorithm on SDSS data and found that their

approach provides solid estimates even for extremely faint stellar systems. The isocontours plotted in the top panel of Figure 8 display quite clearly that the spatial distribution of the galaxy is quite spherical and symmetrical. The coordinates of the galaxy center (see labeled values in the top panel of Figure 8 and values listed in Table 4) are in fair agreement with the estimate based on the 3D histogram. The isocontours plotted in this panel display quite clearly the presence of candidate galaxy stars at radial distances larger than 1°. Similar evidence was also found by Zhang et al. (2021), but the current evidence is based on a larger sample. Moreover, the maximum likelihood solution suggests a position angle of $\theta \sim 75^{\circ}$, a very modest eccentricity ($\epsilon \sim 0.15$), and $R_{\text{half}} = 10.2$. The current structural parameters are quite consistent with those provided by Zhang et al. (2021; orange dotted ellipse in the figure) for the intermediate and old stellar tracers (RGB plus RC stars). They found a similar mean position angle ($\theta = 62^{\circ}$), but their mean eccentricity is a factor of three larger (0.35 vs. 0.15) and their half-light radius is greater than our solution (16.13 vs. 10/20). They also provided the variation of both the position angle and the ellipticity as a function of the major-axis radius (see their Figure 8). They found that θ decreases from 80° to 35° when moving from the innermost (r = 0.2) to the outermost ($r = 0^{\circ}9$) galactic regions, while the eccentricity in the same regions increases from 0.2 to 0.4. These findings agree quite well with results obtained by Battinelli et al. (2006), suggesting a variation in θ from 80° $(r \sim 0.1)$ to 65° $(r \sim 0.6)$ and in ϵ from \sim 0.20 to \sim 0.38. In passing, we note that the difference in eccentricity and in half-light radius, based on the maximum likelihood solution and similar estimates in the literature, is mainly due to the depth and homogeneity of the current photometric catalog across the main body of the galaxy. To constrain on a more quantitative basis the difference, we performed a new estimate of the structural parameters by selecting two different star samples. The first sample was made considering all the stars with 20.75 mag < i < 23.5 mag and g - i > 0.5 mag; the second sample was obtained by artificially cutting the photometric catalog to stars brighter than i =23.5 mag. The results are plotted in the middle and bottom panels of Figure 8 and show that the isocontours and the structural parameters remain very similar to the global solution.

5. Stellar Populations in NGC 6822

The CMD of NGC 6822 has been already introduced in Sections 2 and 3. We now discuss the different stellar populations present in the galaxy and their evolutionary and structural properties. Note that in the following we focus our attention only on the catalog of candidate galaxy stars discussed in Section 3.

5.1. Young, Intermediate, and Old Stellar Tracers

The left panel of Figure 9 shows the *i*, *g*–*i* CMD of candidate NGC 6822 stars. Note that this CMD covers more than nine *i*-band magnitudes and shows several well-defined evolutionary phases, associated with young, intermediate, and old stellar populations. On the basis of different sets of stellar isochrones covering a broad age range retrieved from the BASTI database¹⁴ and by visual inspection, we selected different

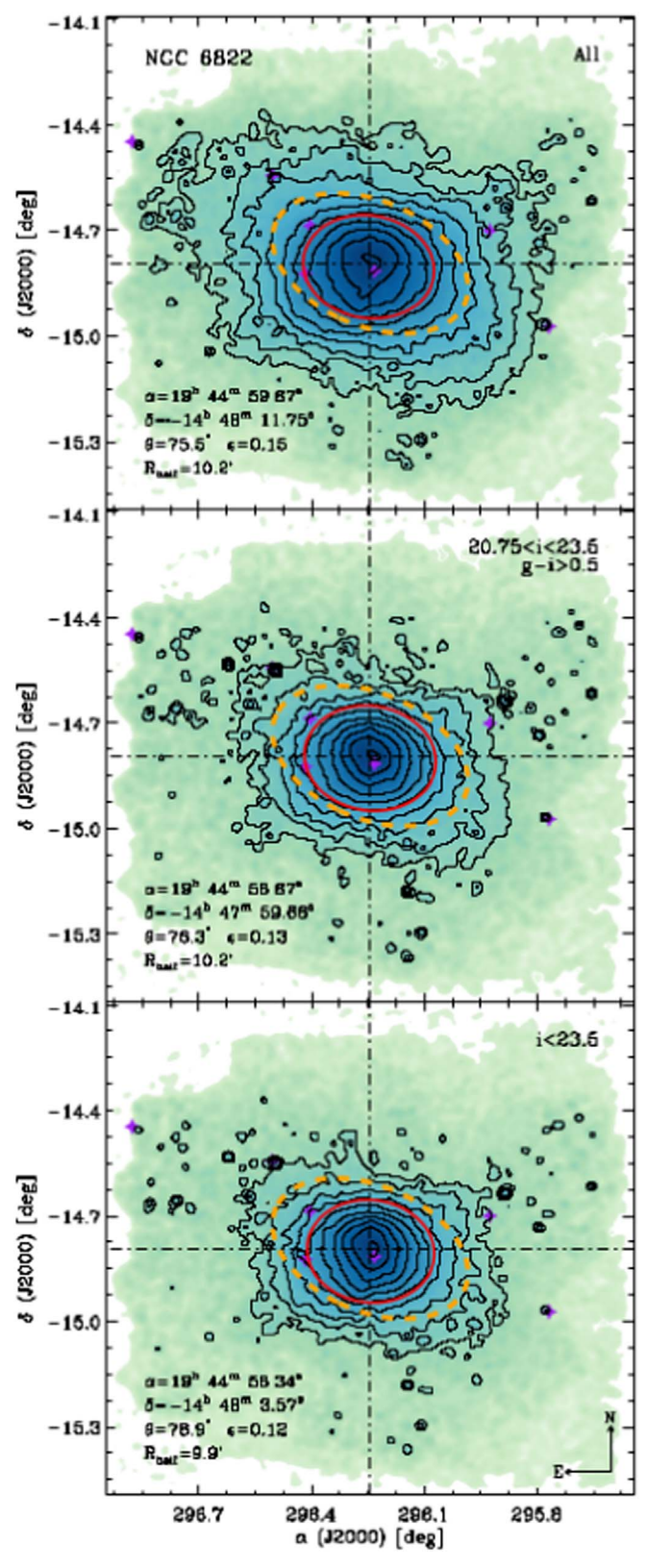


Figure 8. Top: spatial distribution of the entire sample of candidate NGC 6822 stars. The contours display the isodensity levels from 5% to 95% in a logarithmic scale. The red and orange dotted ellipses outline our fit and results from Zhang et al. (2021), respectively. The purple stars show the location of the eight known NGC 6822 GCs (e.g., Hwang et al. 2011; Huxor et al. 2013). Middle: same as the top panel, but the galaxy candidates were selected both magnitude (20.75 mag < i < 23.5 mag) and in color (g - i > 0.5 mag). Bottom: same as the middle panel, but the sample was only selected in magnitude (i < 23.5 mag).

¹⁴ The interested reader is referred to http://basti-iac.oa-abruzzo.inaf.it/index.html.

Table 4
Structural Parameters for the Selected Stellar Tracers

Stellar Tracer	α	δ	θ	ϵ	$R_{ m half}$	Δ R.A.	$\Delta Decl.$
	(J2000)	(J2000)	(deg)		(arcmin)	(arcmin)	(arcmin)
Global ^a	19 ^h 44 ^m 58.56 ^s	$-14^{h}47^{m}34.80^{s}$					
G1 ^b	19h44m58.56s	$-14^{\rm h}47^{\rm m}34.80^{\rm s}$	75.8	0.14	10.2		
G2 ^c	19 ^h 44 ^m 59.67 ^s	$-14^{\rm h}48^{\rm m}11.75^{\rm s}$	75.5	0.15	10.2	-0.28	0.62
G3 ^d	19 ^h 44 ^m 58.67 ^s	$-14^{\rm h}47^{\rm m}59.66^{\rm s}$	76.3	0.13	10.2	-0.03	0.41
G4 ^e	19h44m58.34s	$-14^{\rm h}48^{\rm m}3.57^{\rm s}$	78.9	0.12	9.9	0.06	0.48
MS+RSG	19 ^h 44 ^m 56.73 ^s	$-14^{\rm h}48^{\rm m}50.20^{\rm s}$	-28.7	0.36	6.3	0.46	1.26
RC	19h44m58.80s	$-14^{\rm h}48^{\rm m}36.00^{\rm s}$	67.1	0.22	11.8	-0.06	1.02
TRGB	19 ^h 44 ^m 57.63 ^s	$-14^{\rm h}48^{\rm m}12.62^{\rm s}$	82.4	0.12	13.9	0.23	0.63
RGB2	19h44m58.15s	$-14^{\rm h}48^{\rm m}0.76^{\rm s}$	71.3	0.12	10.1	0.10	0.43
O-rich	19 ^h 44 ^m 56.13 ^s	$-14^{\rm h}48^{\rm m}26.01^{\rm s}$	89.4	0.13	12.4	0.61	0.85
C-rich	19 ^h 44 ^m 54.45 ^s	$-14^{h}48^{m}48.22^{s}$	104.3	0.08	4.9	1.03	1.22

Notes. From left to right the columns give the stellar tracer, sky coordinates of the galaxy center, the position angle, the eccentricity, the half-light radius, and difference in R.A. and decl. with the galaxy center estimated in Section 4 (see also Figures 16 and 17).

stellar tracers, highlighted with circles of different colors (see labels). We focus our attention on the following stellar tracers.

Young stellar tracers.—YMS (violet circles) was selected considering stars with i < 23 mag and -0.5 mag < g - i < 0.3 mag. Note that the fainter limit in magnitude was fixed at i = 23 mag to avoid possible contamination of old and intermediate-age helium-burning stars (HB, RC). Moreover, we also selected RSGs (blue circles) located between 16 mag < i < 20.5 mag and 1.4 mag < g - i < 2.6 mag. We selected these evolutionary phases because NGC 6822 is, together with IC 10, the prototype of star-forming galaxies identified at high redshifts. Indeed, photometric and spectroscopic investigations indicate that NGC 6822 has recently experienced several star formation episodes.

Intermediate stellar tracers.—RC (cyan circles) stars were selected in the region located at 23.7 mag < i < 24.3 mag and 0.8 mag < g - i < 1.2 mag. RC stars are central heliumburning stars, and their stellar masses are intermediate between the low-mass $(M/M_{\odot} \leq 1.2)$ stellar structures characterized by helium cores strongly affected by electron degeneracy and the intermediate-mass ($M/M_{\odot} \geqslant 2.3$) stars that ignite quiescently central helium burning. The limits in stellar mass of the evolutionary channel producing RC stars depend on the chemical composition, and their key feature is to ignite helium in a partially electron-degenerate helium core. The identification of the peak associated with RC stars is based on several tests and trials on 3D histograms (i, g-i, N [number of stars], r, g-i, N). Data plotted in this CMD show that RC stars overlap with RG stars. This degeneracy is caused by the so-called agemetallicity degeneracy along the RGB. Indeed, RG stars associated with stellar populations covering a broad range in age and/or chemical composition cover, at fixed magnitude, a broad range in colors over the entire RGB. Note that in the magnitude range typical of RC stars the thickness in g-i color of the RGB is of the order of 1 mag. However, the identification of RC stars is facilitated by the empirical and theoretical evidence that the central helium-burning lifetime of RC stars is systematically longer than the hydrogen shell burning lifetime along the RGB. This means that the quoted 3D

histograms display a well-defined peak in magnitude and in color across the RC region (see Appendix A).

In this group we also included AGB (dark-green circles) stars, and they were selected as the stars brighter than the TRGB ($i \sim 20.3$ mag) and redder than the RSGs. Note that AGB stars are a mixed bag, given that all stellar populations older than ≈ 0.5 Gyr produce AGB stars. However, in stellar systems, like NGC 6822, that experienced recent star formation events, AGB stars are typically dominated by intermediatemass ($2 \le M/M_{\odot} \le 8$) stellar structure. In passing, it is worth mentioning that the current criteria are only able to select bright AGB stars; indeed, the AGB stars fainter than the TRGB (early AGB) in the optical CMD overlap with RGB stars, and they can be hardly identified.

Old stellar tracers.—Theory and observations indicate that TRGB stars attain a constant i-band magnitude over a broad range of stellar ages and chemical compositions. The TRGB was identified, following Sanna et al. (2008) and Bono et al. (2008), by using both the *i*-band luminosity function and the 3D histogram (i, g-i, N), and we found that its apparent magnitude and color are $i \sim 20.32 \pm 0.01$ mag, $g-i \sim$ 1.68 ± 0.01 mag. TRGB stars (red circles) were selected as the stars located between the TRGB and 0.7 mag fainter. We are aware that this region of the CMD includes RG stars associated with intermediate-age stellar populations. However, their contribution, if we assume a homogeneous star formation rate over the age range producing RG stars and an initial mass function a la Salpeter (power law), is modest when compared with truly old ($t \ge 10 \,\text{Gyr}$) stellar populations. Moreover, stellar populations with a chemical composition typical of NGC 6822 ([Fe/H] = -1.05; Kirby et al. 2013) stellar structures with masses larger than 2.1 M_{\odot} are beyond the so-called red giant transition (Sweigart et al. 1989, 1990). This means that they ignite quiescently central helium burning and the extension in magnitude and in color of their RG branches is quite modest when compared with truly old stellar structures. However, to take account of the change in the stellar populations that are distributed along the RGB, we also selected a fainter RGB region (RGB2; orange circles) located between the TRGB and

^a Estimate of galaxy center based on the 3D histogram of older stellar tracers (see Figure 7).

b Maximum likelihood performed over the entire sample of NGC 6822 candidate stars, but assuming the galaxy center based on the 3D histogram.

^c Maximum likelihood performed over the entire sample of NGC 6822 candidate stars, but keeping all the parameters free (see the top panel of Figure 8).

^d Maximum likelihood performed by selecting candidate galaxy stars in magnitude (20.75 mag < i < 23.5 mag) and in color (g - i > 0.5 mag; see the middle panel of Figure 8).

^e Maximum likelihood performed by selecting candidate galaxy stars in magnitude (i < 23.5 mag; see the bottom panel of Figure 8).

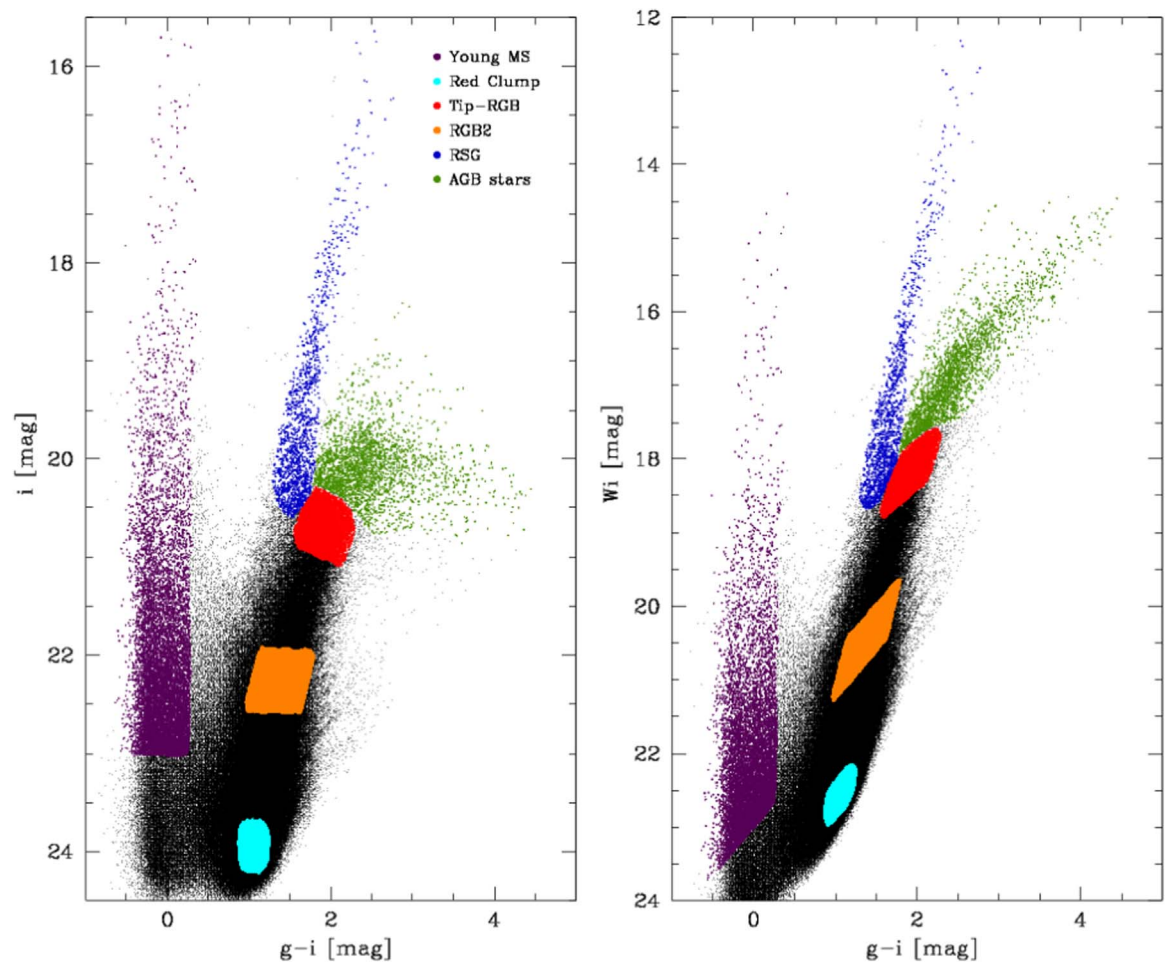


Figure 9. Left: i, g–i CMD of candidate NGC 6822 stars. Young (MS, RSG), intermediate (RC, AGB), and old (TRGB, RGB2) stellar tracers are marked with circles of different colors (see labels). Right: same as the left panel, but using the reddening-free pseudo-magnitude called Wesenheit index W_i , defined as $W_i = i - 1.32$ (g - i) mag.

the RC region: 22 mag < i < 22.5 mag and 1 mag < g - i < 1.6 mag. Note that the range in color covered by RGs in the RGB2 sample is wider than for stars in the TRGB sample, thus further supporting degeneracy between metallicity and age.

The criteria adopted to select the different stellar tracers rely on apparent magnitudes and on colors. Therefore, they are affected by possible systematics because NGC 6822 is affected by differential reddening. To validate the criteria adopted for selecting the different populations, we plotted the same stars by using the so-called Wesenheit index (van den Bergh 1968; Madore 1976; Bono et al. 2010a, 2019). The reason is twofold: (i) The Wesenheit index is a pseudo-magnitude that is reddening-free by construction. This means that it is independent of reddening and of differential reddening. (ii) It can be derived by using measurements in two different bands. However, the Wesenheit magnitude is also affected by two main drawbacks: (i) it relies on the assumption that the reddening law is universal; (ii) the intrinsic error is larger than the typical error affecting single band magnitudes. We defined the i-band Wesenheit magnitude by using the reddening law provided by Cardelli et al. (1989) and the central wavelengths of the Pan-STARRS photometric system (Tonry et al. 2012). In particular, we found $W_i = i - 1.32(g - i)$ mag. The right panel of Figure 9 shows the stellar populations selected in the left panel and with the same color-coding. Note that in this CMD the reddening and the differential reddening can only affect the

spread in color. Data plotted in this panel show that the use of the Wesenheit index, taking account of the color information, further improves the definition of several evolutionary phases. Candidate AGB stars cover more than three Wesenheit magnitudes, and they are distributed along a well-defined and narrow sequence. The RSG sequence is narrower than in the *i*, *g*–*i* CMD and fully supports the cuts in magnitude and colors adopted to separate RSG and AGB stars. The boxes adopted for selecting TRGB, RGB2, and RC stars are, as expected, slanted toward brighter magnitudes. Redder stars, at fixed magnitude, become systematically brighter in Wesenheit magnitude. As a whole they display similar features, thus suggesting that differential reddening plays a minor role in the selection of the different stellar tracers.

5.1.1. Near-infrared and Mid-Infrared Magnitudes

The Wesenheit magnitude allowed us to constrain the impact that reddening and differential reddening have on the magnitude adopted for selecting the different stellar tracers. However, the g-i color is almost a factor of two more sensitive to reddening uncertainties than typical optical colors ($E(B - V)/E(g - i) \sim 0.63$; Cardelli et al. 1989). To investigate on a more quantitative basis the reddening impact on the selection criteria, we decided to take advantage of the NIR and MIR catalogs introduced in Section 2. The NIR data set includes

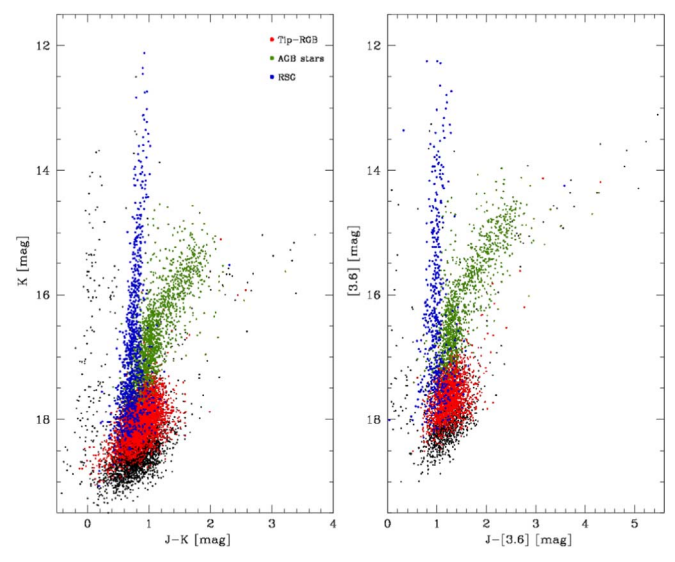


Figure 10. Left: NIR *K*, *J*–*K* CMD for the bright stellar populations (RSGs, AGB stars, TRGB) in NGC 6822. The color-coding is the same as in Figure 9. Right: same as the left panel, but for the NIR–MIR [3.6], *J*–[3.6] CMD.

photometric measurements in J, H, K bands down to limiting magnitudes of \sim 20.6, \sim 20.0, and \sim 19.6 mag, respectively (S12). The MIR photometry based on Spitzer images (Khan et al. 2015) includes measurements in the IRAC bands, and their limiting magnitudes are either similar to or slightly brighter than the NIR catalog. We cross-correlated the three different catalogs and ended up with an optical–NIR–MIR catalog including \sim 97,500 stars with at least one optical and one NIR magnitude and \sim 30,023 stars with at least one optical and one MIR magnitude.

Data plotted in the left panel of Figure 10 show the NIR K, J-K CMD of the bright stellar populations in NGC 6822. The evolutionary sequences for RSGs and AGB stars are quite narrow in color and cover a wide range in magnitudes. Moreover, RSGs and AGB stars display a clear separation for $K \leq 16.5$ mag. However, TRGB stars are distributed over a range of 2 mag in K and 1 mag in J-K and overlap with RSGs and AGB stars. This means that the separation among the three different stellar tracers in this NIR CMD is prone to possible systematics. The right panel of the same figure shows the NIR–MIR [3.6], J-[3.6] CMD for the same stellar tracers. The separation between RSGs and AGB stars becomes clearer down to [3.6] \sim 17 mag, but the mix of the three different stellar tracers at fainter magnitudes is still present.

Data plotted in NIR and in NIR–MIR CMDs are hampered by the limited sensitivity of these colors to the effective temperature. The g–i color is more sensitive to the effective temperature than NIR and NIR–MIR colors, but it is significantly smaller than optical–NIR and optical–MIR colors. Indeed, the difference in color between RSG, TRGB, and bright AGB stars is of the order of 3 mag in g–i, but it becomes of the order of 7 mag in g–K and 8 mag in g–i, but it becomes of the order of 7 mag in g–K and 8 mag in g–i, but it becomes of the order of 7 mag in g–K and 8 mag in g–i, but it becomes of the order of 7 mag in g–K and 8 mag in g–i, but it becomes of the order of 7 mag in g–K and 8 mag in g–i, but it becomes of the order of 7 mag in g–K and 8 mag in g–i, but it becomes of the order of 9 mag in g–i, but it becomes of the order of 9 mag in g–i, but it becomes of the order of 9 mag in g–i, but it becomes of the order of 9 mag in g–i, but it becomes of the order of 9 mag in g–i, but it becomes of the order of 9 mag in g–i, but it becomes of the order of 9 mag in g–i, but it becomes of the order of 9 mag in g–i, but it becomes of the order of 9 mag in g–i, but it becomes of the order of 9 mag in g–i, but it becomes of the order of 9 mag in g–i, but it becomes of the order of 9 mag in g–i, but it becomes of the order of 9 mag in g–i, but it becomes of the order of 9 mag in g–i, but it becomes of the order of 9 mag in g–i, but it becomes of the order of 9 mag in g–i, but it becomes of the order of 9 mag in g–i, but it becomes of the order of 9 mag in g–i, but it becomes of the order of 9 mag in g–i, but it is significantly and g–i, but it becomes of the order of 9 mag in g–i, but it is significantly and g–i, but it is significantl

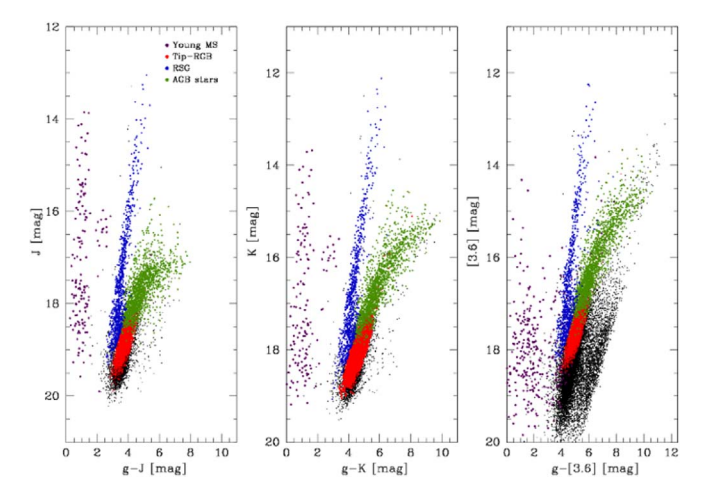


Figure 11. Same as Figure 9, but young (MS, RSG), intermediate (AGB), and old (TRGB) stellar tracers are plotted in the two optical–NIR J, g–J (left) and K, g–K (middle) CMDs and in the optical–MIR [3.6], g–[3.6] CMD (right). The color-coding is the same as in Figure 9.

defined sequences and cover a very broad range in magnitudes and in colors.

Data plotted in this figure display several interesting features worth discussing in more detail. (i) AGB and TRGB stars overlap over a substantial range in magnitude from 0.3 to 0.4 mag in the Jband, from 0.5 to 0.6 mag in K, and from 0.8 to 0.9 mag in [3.6]. This means that photometric selections only based on optical/ NIR/MIR CMDs are, once again, prone to systematics, since TRGB and AGB stars cover similar magnitude and colors. The same outcome applies to the separation between RSGs and TRGB stars. (ii) AGB stars cover more than 3 mag in [3.6] and 6 mag in g-[3.6] color, thus providing a firm validation for the separation of cool and warm AGB stars. (iii) YMS stars (violet circles) are also present, but only the very bright massive stars have been detected. The current empirical evidence indicates that the optical/NIR/ MIR CMDs concerning young and intermediate-age stellar tracers bring forward several advantages (reduced sensitivity to reddening and differential reddening, strong sensitivity to effective temperature) when compared with NIR and optical CMDs, but they are affected by systematics when dealing with old stellar tracers.

5.2. AGB: Selection of C- and O-rich Stars

We focused our attention on AGB stars because they cover a broad range in stellar masses ($M \sim 1-8 M_{\odot}$) and, in turn, stellar ages (from a few hundred Myr to more than 10 Gyr). This means that their spatial distributions can be safely adopted to trace back in time and in space the star formation episodes experienced by stellar systems. The AGB stars are classified according to their carbon-to-oxygen abundance ratios in three different groups: C type (C/O > 1), O type (C/O < 1), also called M type), and S type (C/O \sim 1). Several subclasses have more recently been suggested, and the reader interested in a more detailed discussion is referred to Boyer et al. (2011, 2015). Photometric and spectroscopic investigations indicate that C- and O-type stars typically display different radial distributions, with the latter ones more centrally concentrated than the former ones. This means that a comprehensive analysis of O-rich and C-rich AGB stars covering the entire body of the galaxy will provide solid constraints on their dependence on the environment and on their metallicity distribution.

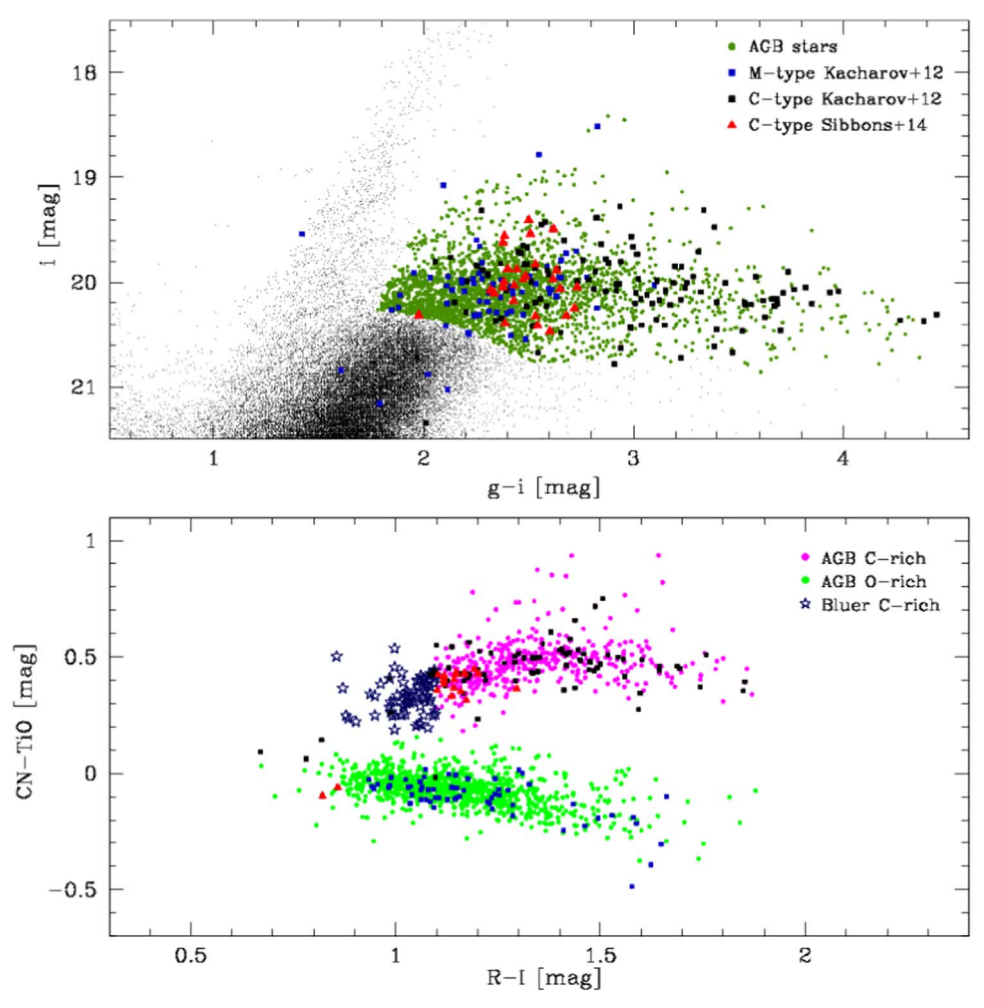


Figure 12. Top: *i*, *g*–*i* CMD of candidate AGB stars in NGC 6822. The CMD is zoomed in on the bright portion to show the current AGB sample (dark-green circles). Blue squares and red triangles display spectroscopically confirmed C-type stars (K12; S12), while black squares show confirmed M-type stars (K12). Bottom: CN–TiO, *R*–*I* CCD for candidate AGB stars plotted in the top panel. The diagram is based on multiband photometry collected by L02 and shows a clear separation between candidate C-rich (magenta circles) and O-rich (green circles) stars. The blue star symbols highlight the so-called bluer C stars, as defined by L02. Symbols and colors of the spectroscopic sample (C-, M-type) are the same as the top panel.

We have already mentioned in Section 5.1 that candidate AGB stars were selected in the i, g-i CMD (see Figure 9) as the stars brighter than the TRGB ($i \sim 20.3$ mag) and redder than the RSGs. The top panel of Figure 12 shows in the same CMD a zoom-in of the entire sample of candidate AGB stars (2788 stars; dark-green circles). To further support the photometric selection of AGB stars, we took advantage of the spectroscopic catalogs of C- and M-type stars available in the literature for NGC 6822. A detailed spectroscopic investigation was performed by K12. They used low-resolution spectra collected with the multiobject slit spectrograph VIMOS at VLT (ESO) and identified 150 C-type stars and 122 M-type stars. A similar spectroscopic analysis was also performed by S12, who provided a sample of 82 C-type stars and one anomalous M-type giant by using the AAOmega multifiber spectrograph at the Anglo-Australian Telescope (AAT). The spectroscopic catalogs were cross-matched with our optical catalog, and the objects in common are plotted in the top panel of Figure 12. The C-type stars identified by K12 are shown with black squares, while those identified by S12 are shown with red triangles; the M-type stars identified by K12 are plotted as blue squares. A glance at the data plotted in this panel shows that candidate AGB stars selected by using photometric properties

agree quite well with spectroscopically selected samples. The photometric sample, as expected, outnumbers the spectroscopic sample, but they cover similar magnitude and color ranges. Note that spectroscopic M-type stars attain, as expected, colors that are systematically bluer than C-type stars. However, the two subgroups are degenerate in the i, g-i CMD because they display a clear separation neither in magnitude nor in color. In passing, we also note that we investigated the few outliers located in regions typical either of the RGs or of the RSGs. We found that they have close companions and the cross-match was not univocal, i.e., there is the presence of multiple stars within the typical searching radius (1'').

Spectroscopic samples of C- and O-rich stars are based on solid diagnostics, but they are limited to the central regions of a stellar system and quite often hampered by modest statistics. To overcome these limitations we decided to use the sample of candidate C- and O-rich stars provided by L02. The key advantage of their approach is that they use a mix of broad (*R*, *I*) and narrow (CN, TiO) band photometry for the identification of candidate C- and O-rich stars. In their investigation on AGB stars in NGC 6822 they used multiband photometry collected with both the Swope telescope and the wide-field imager CFH12K at CFHT. They identified 904 candidate C-type stars,

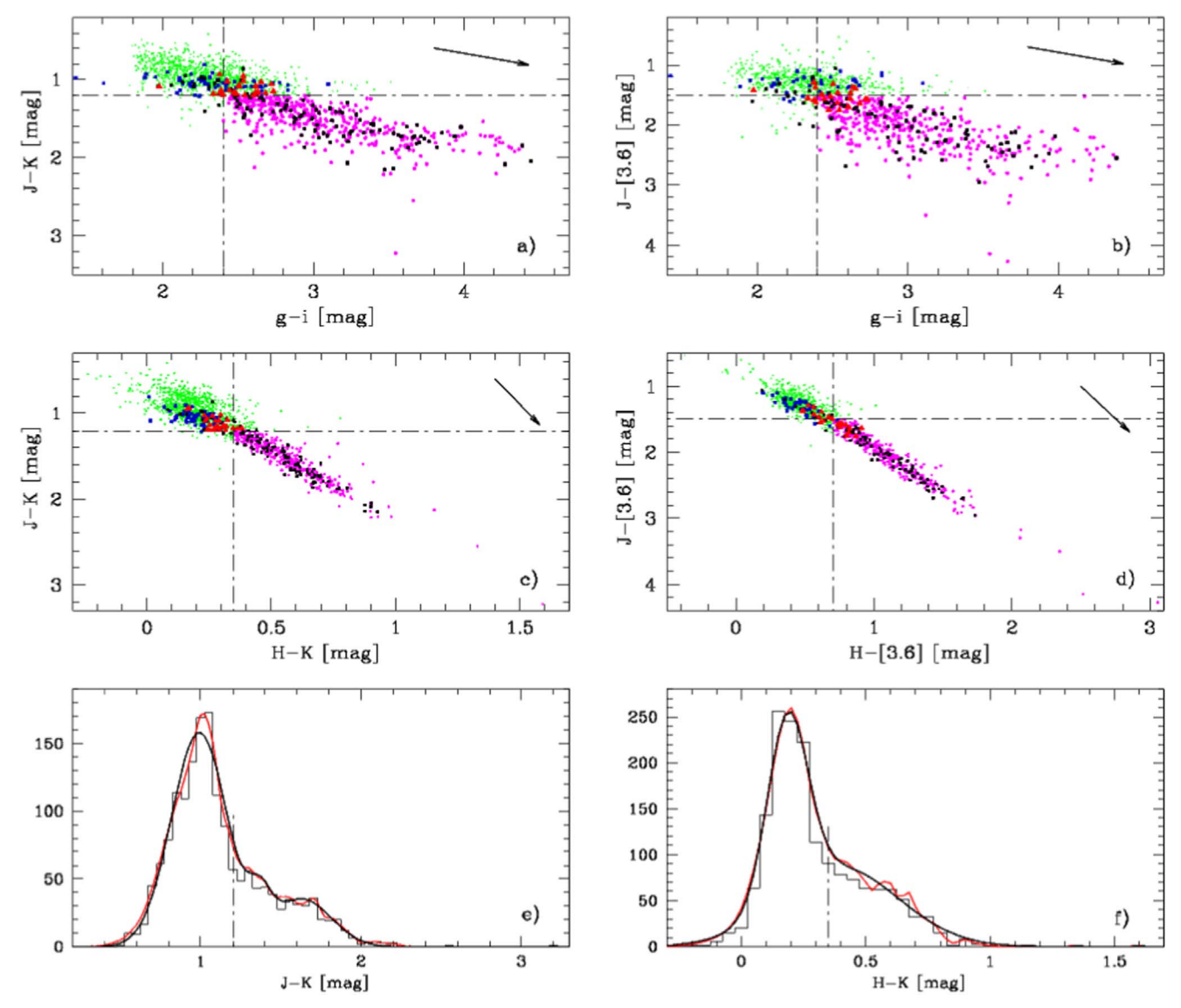


Figure 13. (a) Optical–NIR (J–K–g–i) CCD for candidate AGB stars plotted in the top panel of Figure 12. The dotted–dashed lines show the color cuts adopted to separate C-rich (magenta circles) and O-rich stars (green circles). We performed a fit of the different color distributions following the same approach adopted by Kang et al. (2006). See text for more details. Symbols and colors of the spectroscopic sample (C and M type) are the same as in Figure 12. The black arrow plotted in the upper right corner displays the reddening vector for an arbitrary extinction value. (b) Same as panel (a), but for optical–NIR–MIR (J–[3.6]–g–i) CCD. Note that the color cuts are different. (c) Same as panel (a), but for NIR (J–K) CCD. (d) Same as panel (a), but for NIR–MIR (J–K) CCD. (e) Histogram in the NIR color J–K of candidate O- and C-rich stars. The thin red line shows the same color distribution, but smoothed with a Gaussian kernel with unitary weight and σ equal to the photometric errors (summed in quadrature) on individual color measurements. The black line shows the multi-Gaussian (three) fit of the smoothed color distribution. The dotted–dashed line shows the color cut at J–K = 1.2 mag. (f) Same as panel (e), but for H–K color distribution. Note that the Gaussian fit was performed by using two Gaussians. The color limit is at H–K = 0.35 mag.

the sample was selected by using sharp cuts in the color-color plane: $(R-I)_0 > 0.90$ mag and (CN-TiO) > 0.3 mag. Note that to unredden the R-I color they used a mean reddening of E (R-I) = 0.20 mag. Although this CCD is a very solid diagnostic for the identification of C-type stars, the identification of O-rich stars is hampered by the contamination of field red giants because they attain similar colors (see Figure 3 in L02).

We have already discussed in Section 3 the approach we adopted to separate candidate field and galaxy stars, and to fully exploit its potential, we cross-correlated their catalog, kindly provided by the authors in electronic form, with our sample of candidate AGB stars. The results of the cross-match are shown in the bottom panel of Figure 12. Once contaminant field stars are removed, the CN–TiO, *R-I* CCD becomes a very solid diagnostic to identify both C-rich (486; magenta circles)

and O-rich stars (1002; green circles). The blue star symbols in figure highlight the so-called "bluer C stars," as defined by L02 (0.8 < (R-I) < 1.1), that we excluded from our sample of candidate C-rich stars because they deserve a more detailed spectroscopic analysis. Note that the number of candidate C-type stars is significantly smaller than the original sample provided by L02 owing to difficulties either in the astrometric solution of the two different data sets or in separating candidate field and galaxy stars. To further validate the current selection of AGB stars, we have also plotted the spectroscopically confirmed C- and M-type stars (same as the top panel of Figure 12). Spectroscopic data plotted in this CCD based on broad- and narrowband photometry clearly show the separation between candidate C- and O-rich stars.

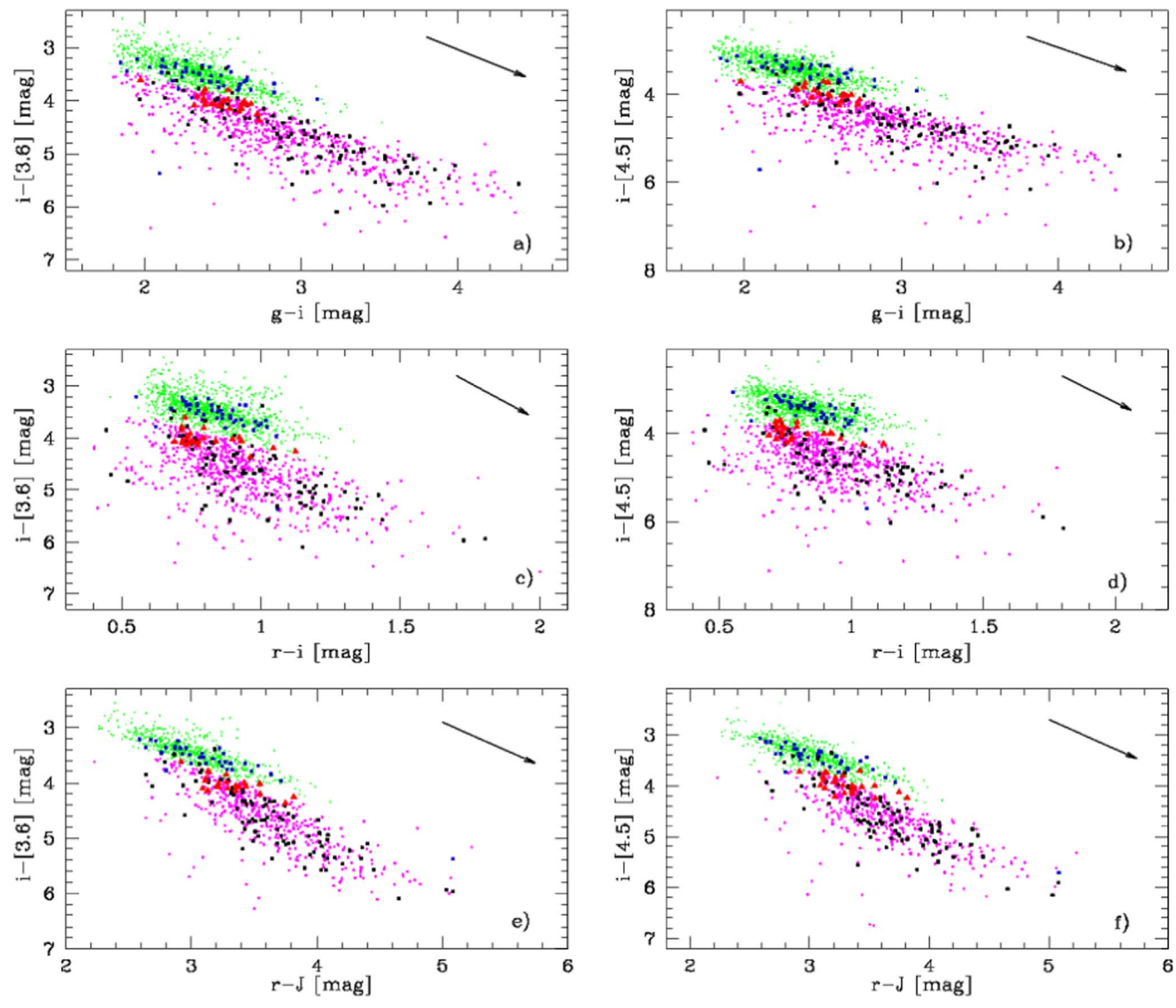


Figure 14. (a) Same as panel (a) in Figure 13, but for optical–MIR (i-[3.6]-g-i) CCD. Note that C- and O-rich candidates are distributed along two different, almost parallel sequences. The C-rich candidates cover more than 3 mag in the optical–MIR, i-[3.6], color and \sim 2.5 mag in the optical, g-i, color. The range in colors covered by O-rich candidates is roughly a factor of two smaller. Symbols and colors of the spectroscopic AGB sample are the same as in Figure 12. The black arrow plotted in the upper right corner displays the reddening vector for an arbitrary extinction value. (b) Same as panel (a), but for optical–MIR (i-[4.5]-g-i) CCD. (c) Same as panel (a), but for optical–MIR (i-[4.5]-r-i) CCD. (d) Same as panel (a), but for optical–MIR (i-[4.5]-r-i) CCD. (e) Same as panel (a), but for optical–MIR CCDs is that C- and O-rich display different slopes. (f) Same as panel (a), but for optical–NIR–MIR (i-[4.5]-r-J) CCD.

To further investigate this long-standing problem of the identification of C- and O-rich stars, we decided to take advantage of the multiband catalog we built up. In this context it is worth mentioning that Kang et al. (2006) have defined a solid photometric approach for selecting candidate C- and O-rich stars by using NIR photometry. In their investigation on NGC 6822 they used the J-K, H-K CCD as a diagnostic to identify C- and M-type stars. They showed that the histograms in NIR colors (J-K, H-K) of candidate AGB stars have a main peak associated with M stars and a long red tail associated with C stars. Following this approach and the NIR color cuts (J-K = 1.53 mag, H-K = 0.5 mag) provided by Davidge (2005), they provided a solid separation between C- and M-type stars in NGC 6822 (see their Figure 7). To take advantage of the current optical/NIR/MIR catalog, we decided to follow a similar approach, but with different criteria to define the color cuts. Data plotted in Figure 13 show selected AGB

stars on different optical–NIR (J-K-g-i; panel (a)), NIR (J-K-g-i; panel (a))H-K; panel (c)), and optical-NIR/MIR (J-[3.6]-g-i, J-[3.6]-g-iH–[3.6]; panels (b) and (d)) CCDs. For each CCD we derived histograms in color (thin gray lines in panels (e) and (f)) and performed a multi-Gaussian fit (black lines) of the smoothed distribution (red solid lines in panels (e) and (f)). The color distribution was smoothed with a Gaussian kernel with unitary weight and σ equal to the photometric errors (summed in quadrature) on individual color measurements. We performed a series of test and trials to define objective criteria for the separation of candidate C- and M-type stars, and eventually we decided to fix the color cuts as the mean between the peaks of primary and secondary Gaussian (black lines in panels (e) and (f)), independently of the number of Gaussians used to fit the global distribution in color. We found the color cuts J-K=1.2, J–[3.6] = 1.5, g–i = 2.4, H–K = 0.35, and H–[3.6] = 0.7, and they are plotted as dashed-dotted lines in the top four panels of

Figure 13. The approach outlined in this section appears quite promising; indeed, the color sequences and the reddening vectors (black arrows) display different slopes. This suggests that the variations in color are intrinsic and only minimally affected by differential reddening. However, this approach is still affected by thorny problems. (i) The NIR, optical/NIR, and optical/NIR/MIR CCDs shown in this figure display welldefined color sequence when moving from M- to C-type stars. This means that they do not show any clear separation, as in the (CN-TiO), (R-I) CCD, and/or a change in the slope. This evidence is further supported by the comparison with the spectroscopic samples. Indeed, several spectroscopic C-type stars attain colors that are more typical of M-type stars and vice versa. (ii) The main peak associated with M-type stars is affected by the contamination of field stars, since they typically have similar colors.

This means that a solid separation between field and cluster stars is required as a preliminary step to the definition of the color cuts.

To overcome these difficulties, we decided to investigate other possible color combinations among the available optical, NIR, and MIR magnitudes for NGC 6822 to search for CCDs that would allow us to better identify C- and M-type stars. A summary of this effort is shown in Figure 14. Data plotted in the optical/MIR CCDs (panels (a)–(d)) clearly show that Cand M-type stars are distributed along two almost parallel sequences. The main difference between the top and the middle panels is that the spread in optical color is, at fixed optical/MIR color (i–[3.6]; left panels; i–[4.5], right panels), significantly smaller in g-i than in r-i. Note that the separation is fully supported by the spectroscopic samples that are distributed along the expected sequences. Moreover, the C-rich sample covers more than 3 mag in optical–MIR colors and from 1.5 (ri) to 2.5 (g-i) mag in optical colors. The O-rich sample covers ranges in optical-MIR and in optical colors that are a factor of two smaller.

The same outcome applies to the optical–NIR–MIR (*i*–[3.6]– *r*–*J* and *i*–[4.5]–*r*–*J*) CCDs plotted in panels (e) and (f) of Figure 14. The key advantage of these CCDs is that sequences associated with O- and C-rich stars display for the first time different slopes. Indeed, the use of an optical/NIR color, together with an optical/MIR color, causes the C-rich sequence to be more slant when compared to optical colors (top and middle panels). Note that optical/NIR colors cover ranges roughly similar to the optical–MIR colors. It is worth mentioning that the slope of C- and O-rich sequences in the quoted CCDs differ from the slope of the reddening vectors (black arrows). This means that the dispersion in color present in all the selected CCDs is an intrinsic feature of the two stellar populations.

The mix of optical/NIR/MIR colors shown in Figure 14 brought forward several key advantages in the identification of C- and M-type stars. Therefore, we decided to investigate the use of these colors to further characterize the sample of C- and O-rich stars. Interestingly enough, we found that CCDs based on two optical–NIR colors (*r*–*K*–*r*–*i*, *i*–*K*–*r*–*i*; top and bottom panels of Figure 15) display the same features of optical/NIR/MIR CCDs, but they also highlight a separation in two parallel sequences of candidate O-rich stars (see the blue and red arrows plotted in the upper left corner of the two panels). Note that spectroscopically confirmed O-rich stars are distributed along the two sequences, but the bluer sequence only includes a

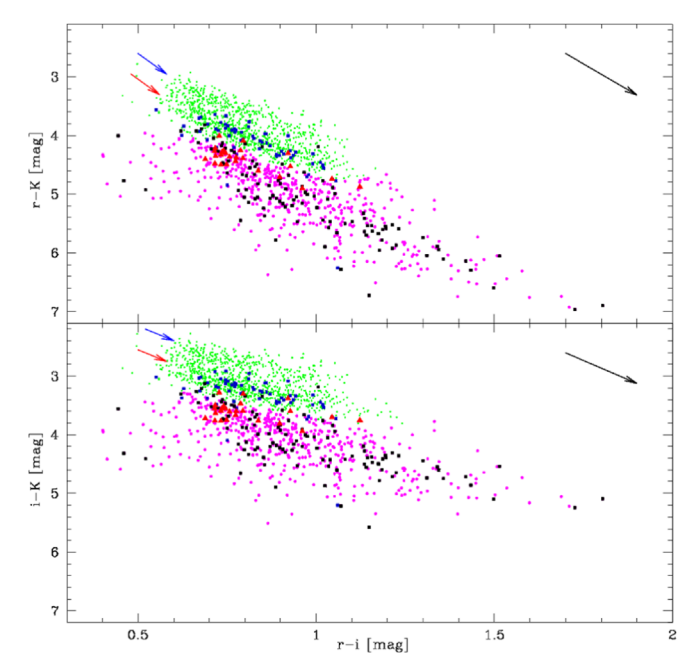


Figure 15. Top: same as panel (a) in Figure 13, but for optical–NIR (r-K-r-i) CCD. The red arrows plotted in the upper left corner display the separation in two different sequences of candidate O-rich stars. Symbols and colors of the spectroscopic AGB sample are the same as in Figure 12. The black arrow plotted in the upper right corner displays the reddening vector for an arbitrary extinction value. Bottom: same as the top panel, but for optical–NIR (i-K-r-i). Note that in this CCD the separation of O-rich candidates into two different sequences is still visible.

few spectroscopic identifications. This empirical evidence indicates that the O-rich stars in NGC 6822 appear to include two different stellar components. Plain physics arguments suggest that the bluer sequence is younger, while the redder sequence is older. More quantitative constraints require a detailed comparison between theory and observations.

The current findings indicate that either optical—NIR (Figure 15) or optical—NIR—MIR (Figure 14) CCDs including either the r or the i band allow us a solid identification and characterization of C- and O-rich stars.

5.3. Radial Distributions of the Different Stellar Tracers

The selection of stellar tracers, covering a broad range of stellar ages, provides the opportunity to investigate on a quantitative basis their radial distributions. To provide quantitative constraints on their structural parameters, we adopted the same algorithm we applied to the global catalog in Section 4. The radial distributions and the isodensity contours of the selected stellar populations are shown in Figures 16 and 17; the results of the fit are overplotted as thick red ellipses, and the structural parameters are also labeled and listed in Table 4.

The top left panel of Figure 16 shows the radial distribution on the sky of young stellar tracers: MS and RSGs. A glance at the isocontours plotted in the top left panel clearly show that young stellar tracers are distributed along a well-defined bar that is mainly located between the first and second quadrants, bending into the fourth quadrant in its southern/southeastern extension. Moreover, and even more importantly, the young bar is systematically off-center (see black dashed-dotted lines and red cross) by 0'.46 in R.A. and 1'.26 in decl. The spatial distribution of young stellar tracers is very similar to the distribution obtained by Hirschauer et al. (2020) for their RSG

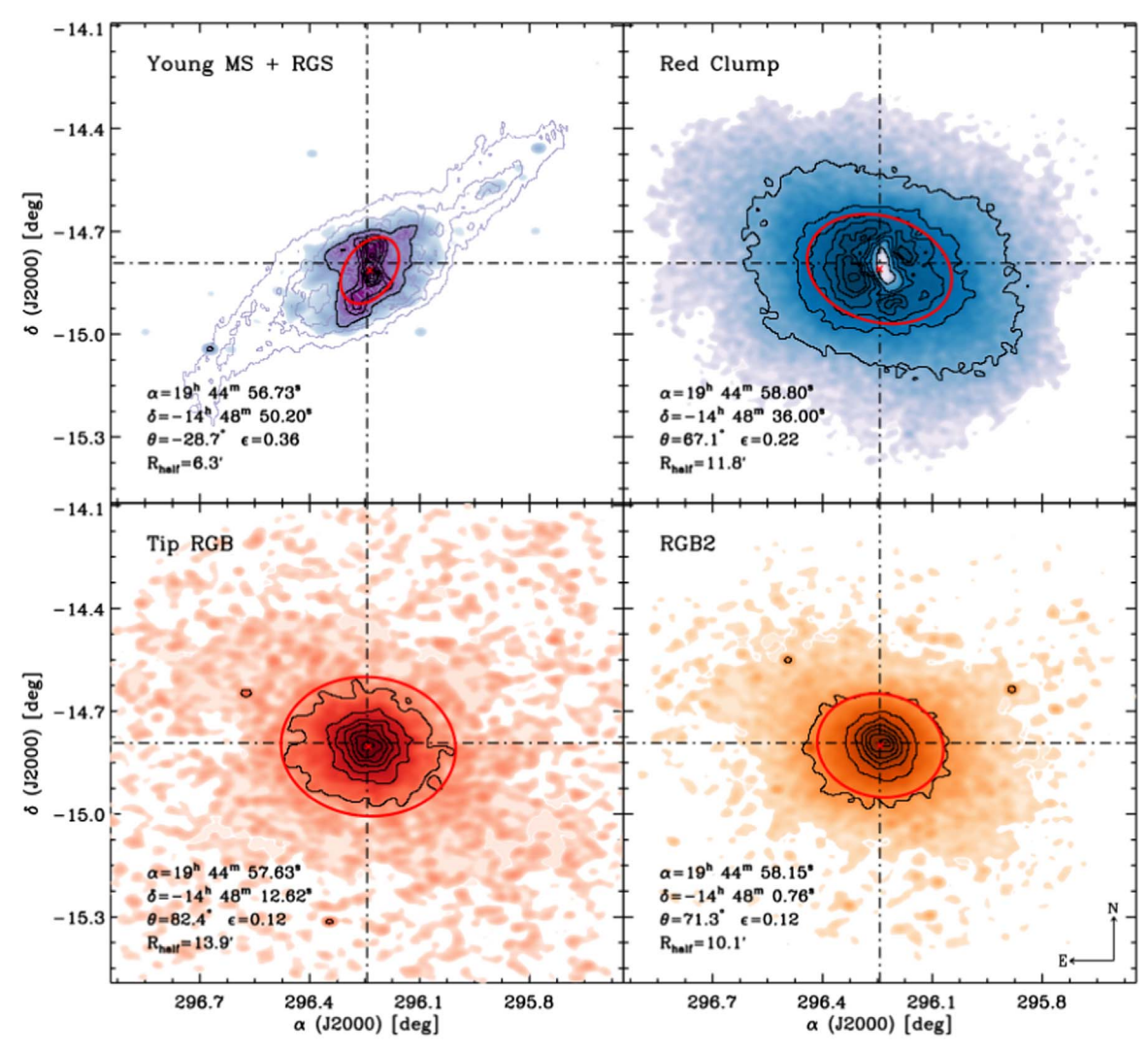


Figure 16. Spatial distributions of the young (YMS + RSG; top left panel), intermediate (RC; top right panel), and old (TRGB, RGB2; bottom panels) stellar tracers in NGC 6822. The contours show the isodensity levels from 5% to 95% in a logarithmic scale. The gray contours plotted in the top left panel (young tracers) highlight the isocontours of the H I column density map from de Blok & Walter (2000, 2003, 2006). The dotted–dashed lines trace the estimated galaxy center (see Section 4). The thick red ellipses outline the fit performed according to the maximum likelihood algorithm by Martin et al. (2008). The derived structural parameters are labeled in the figure and listed in Table 4.

sample. The solution of the fit shows a moderate eccentricity; its position angle is $\theta \sim -29^\circ$, i.e., mainly distributed along the second to fourth quadrants; and it has a modest half-light radius ($R_{\rm half} \sim 6'.3$). The isocontours also suggests that the position angle is driven by young stars located outside the bar, thus suggestive of the possible presence of a disk. This working hypothesis is also supported by the isocontours of the H I column density map obtained by de Blok & Walter (2000, 2003, 2006) and overplotted on the sky distribution of young stars.

The radial distribution of intermediate-age stellar tracers (RC) when compared with young stellar tracers is significantly different (see top right panel of Figure 16). The isocontours are far from being symmetric, and in the innermost regions there is evidence of a steady decrease of RC stars along the bar made by young stars. This is an observational bias. The RC stars are relatively faint ($i \sim 24$ mag), and the innermost galactic regions are more crowded and more affected by internal reddening. This means that our optical catalog is not complete in the innermost regions. To overcome this limitation, we estimated the peak of the RC distribution by performing a Gaussian fit of

the RC distribution in R.A. and decl. (see the red cross). Eventually, we performed the fit, at fixed center position, and the results are plotted in the same panel. The position angle is $\theta \sim 67^{\circ}$, i.e., mainly distributed along the first to third quadrants. Moreover, the solution of the fit indicates a smaller eccentricity ($\epsilon \sim 0.2$), and its half-light radius is almost a factor of two larger. This means that RC stars are distributed over a significant fraction of the body of the galaxy.

The bottom panels of the same figure display the radial distribution of old stellar tracers: TRGB (bottom left) and RGB2 (bottom right). We decided to investigate the radial distribution along the RGB because plain physical arguments outlined in Section 5.1 suggest that the role of old stellar populations increases when moving from fainter (RGB2) to brighter (TRGB) RGs. The solution of the fit for TRGB stars shows an almost spherical distribution ($\epsilon \sim 0.12$) with a position angle of $\theta \sim 82^{\circ}$. This means that old stellar tracers in this galaxy are almost edge-on with the semimajor axis along the E–W direction and the minor axis along the N–S direction. Moreover, and even more importantly, the half-light radius is larger than for young and intermediate-age stellar populations,

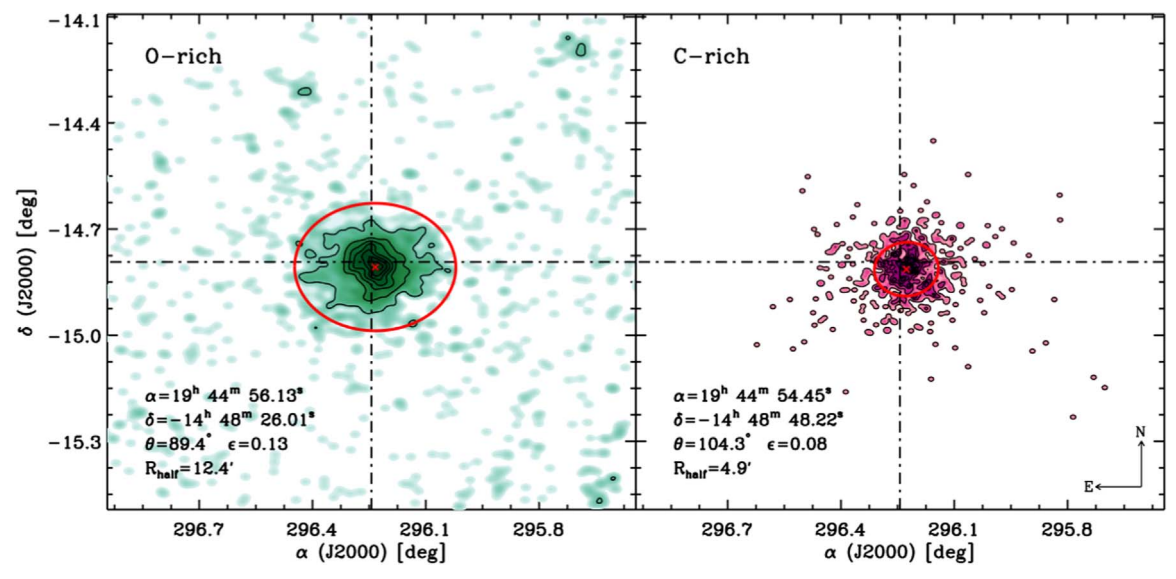


Figure 17. Same as Figure 16, but for O- (left panel) and C-rich (right panel) stars. C-rich stars are based on the selection performed on the r-K-r-i CCD, while the O-rich stars come from our global selection of AGB stars (i, g-i CMD).

and the isocontours cover the entire area covered by our optical photometry. This means that current photometry is not approaching the truncation radius of the galaxy. The radial distribution of the RGB2 plotted in the bottom right panel displays properties that are intermediate between TRGB and RC stellar tracers. Indeed, their eccentricity is almost spherical and similar to old tracers, while the position angle is more similar to the intermediate stellar populations.

AGB stars were closely investigated and characterized; this is the reason why we decide to focus our attention on their spatial distributions (Figure 17). Note that the C-rich stars come from the selection performed on the r-K-r-i CCD because they are the largest sample when compared with the selection performed on the other selected CCDs (see Section 6). The O-rich star sample used here was obtained from our global optical selection of AGB stars (i, g-i CMD) once C-rich stars were removed. As expected, the M-type stars (left panel) show an almost spherical distribution, and their structural parameters are very similar to the structural parameters of the old stellar tracers (bottom panels of Figure 16). The similarity applies not only to the position angle and eccentricity but also to half-light radius, thus suggesting that M-type stars are dominated by old and intermediate-age progenitors. On the other hand, C-rich stars (right panel) are centrally concentrated, and the peak of their distribution is off-center by 1.03 (R.A.) and 1.22 (decl.). This means that their distribution resembles the properties of the young stellar tracers ($R_{\text{half}} = 4.9 \text{ vs. } 6.3$). However, they are spherically distributed ($\epsilon \sim 0.08$) as the old tracers, thus suggesting the key role of low-mass stars for this stellar tracer. The results of the radial distributions for O- and C-rich stars are consistent with those obtained by Hirschauer et al. (2020).

6. Population Ratio between C- and O-rich Stars

The ratio between C- and M-type stars in a stellar population is used as a population diagnostic and to estimate the metallicity of the environment from which AGB stars formed. The reason why the C/M ratio is quite important for a quantitative analysis of resolved stellar populations is twofold. (i) During the AGB phase, low- and intermediate-mass stellar structures experience several physical mechanisms (third

dredge-up, convective overshooting, mass loss, hot bottom burning) affecting the surface chemical composition. The efficiency of these mechanisms depends on several physical parameters and, in particular, on the stellar mass and the chemical composition. Metal-poor and metal-intermediate stellar systems are fundamental laboratories to trace the transition from M- to C-type stars. The reader interested in a more quantitative discussion is referred to Weiss & Ferguson (2009).

(ii) AGB stars are among the most important contributors to the integrated light of a galaxy (Renzini & Buzzoni 1986). Their role becomes even more relevant in the NIR regime, where the effects of dust obscuration are significantly reduced compared to the optical bands. Moreover, and even more importantly, AGB stars play a key role in the chemical enrichment of galaxies, since they produce CNO and neutron capture (*s*-process) elements.

We paid special care to the selection of C- and O-rich stars, and the C/M ratios based on the star counts performed on a wide range of CCDs are listed in Table 5. Note that the table includes C/M ratios based on CCDs that were not discussed in Section 5.2 because they display features similar to the CCDs shown in Figures 14 and 15. They were included to further constrain possible systematics in the use of CCDs based on different optical/NIR/MIR photometric bands. The radial distributions of candidate C- and M-type stars discussed in Section 5.3 show that the former group is significantly more centrally concentrated than the latter one. Moreover, optical, NIR, and MIR data sets cover different galaxy regions (see Section 2). This means that star counts of AGB stars based on optical/NIR/MIR CCDs are sampling different regions of the galaxy. Figure 18 shows the radial distributions of candidate Cand M-type stars selected on the r-K-r-i CCD, together with the sky area covered by MIR images collected with Spitzer (dashed black box). To provide homogeneous and accurate star counts of AGB stars, we performed the selection over a box of 1000 arcsec² located across the center of the galaxy (solid black box).

The number of C- and M-type stars selected by using optical/NIR/MIR CCDs and the C/M ratios are listed in

Table 5

C/M Population Ratios Based on a Variety of Optical/NIR/MIR Color–Color Diagrams and Iron Abundances Based on Empirical C/M Ratio–Metallicity Relations

C-rich	O-rich	C/M	(Fe/H) ^a	(Fe/H) ^b
(C- and O-rich Star Count	s over a Central Area of 1000	arcsec ²	
486	1002	0.49 ± 0.04	-1.14 ± 0.10	-1.24 ± 0.09
467	903	0.52 ± 0.04	-1.15 ± 0.10	-1.26 ± 0.09
454	743	0.61 ± 0.05	-1.19 ± 0.09	-1.29 ± 0.09
460	910	0.51 ± 0.04	-1.15 ± 0.10	-1.25 ± 0.09
461	736	0.63 ± 0.05	-1.20 ± 0.09	-1.30 ± 0.08
546	824	0.66 ± 0.05	-1.21 ± 0.09	-1.31 ± 0.08
605	764	0.80 ± 0.06	-1.26 ± 0.08	-1.34 ± 0.07
588	780	0.75 ± 0.06	-1.25 ± 0.08	-1.33 ± 0.08
755	1053	0.70 ± 0.05	-1.23 ± 0.09	-1.32 ± 0.08
662	1145	0.58 ± 0.04	-1.18 ± 0.09	-1.28 ± 0.09
701	1107	0.63 ± 0.04	-1.20 ± 0.09	-1.30 ± 0.08
714	1095	0.65 ± 0.04	-1.21 ± 0.09	-1.30 ± 0.08
680	1127	0.60 ± 0.04	-1.19 ± 0.09	-1.29 ± 0.09
686	1121	0.61 ± 0.04	-1.19 ± 0.09	-1.29 ± 0.08
520	677	0.77 ± 0.06	-1.25 ± 0.08	-1.34 ± 0.07
494	703	0.70 ± 0.06	-1.23 ± 0.09	-1.32 ± 0.08
C- and O-ric	h Star Counts Made Con	sidering the Entire Area Cover	red by Our Data Set	
482	1186	0.41 ± 0.03	-1.09 ± 0.11	-1.21 ± 0.10
474	1193	0.40 ± 0.03	-1.09 ± 0.11	-1.20 ± 0.10
561	1106	0.51 ± 0.04	-1.15 ± 0.10	-1.25 ± 0.09
624	1041	0.60 ± 0.04	-1.19 ± 0.09	-1.29 ± 0.09
607	1058	0.57 ± 0.04	-1.18 ± 0.09	-1.28 ± 0.09
	486 467 454 460 461 546 605 588 755 662 701 714 680 686 520 494 C- and O-ric 482 474 561 624	C- and O-rich Star Count 486 1002 467 903 454 743 460 910 461 736 546 824 605 764 588 780 755 1053 662 1145 701 1107 714 1095 680 1127 686 1121 520 677 494 703 C- and O-rich Star Counts Made Con 482 1186 474 1193 561 1106 624 1041	C- and O-rich Star Counts over a Central Area of 1000 486 1002 0.49 ± 0.04 467 903 0.52 ± 0.04 454 743 0.61 ± 0.05 460 910 0.51 ± 0.04 461 736 0.63 ± 0.05 546 824 0.66 ± 0.05 605 764 0.80 ± 0.06 588 780 0.75 ± 0.06 755 1053 0.70 ± 0.05 662 1145 0.58 ± 0.04 701 1107 0.63 ± 0.04 714 1095 0.65 ± 0.04 680 1127 0.60 ± 0.04 686 1121 0.61 ± 0.04 520 677 0.77 ± 0.06 494 703 0.70 ± 0.06 C- and O-rich Star Counts Made Considering the Entire Area Cover 482 1186 0.41 ± 0.03 474 1193 0.40 ± 0.03 561 1106 0.51 ± 0.04 624	C- and O-rich Star Counts over a Central Area of 1000 arcsec 2 486

Notes. Iron abundances are based on the current C/M population ratios and the empirical relations provided by

Table 5. The errors on the C/M ratios take account of the Poisson uncertainties. The population ratios listed in this table show that the C/M ratio remains consistent, within the errors, when moving from selections based either on NIR (J-K-H-K), $C/M = 0.51 \pm 0.04$) or on optical/NIR (J-K-g-i, C/M = 0.52 ± 0.04) to a selection based on narrow- and broadband photometry (CN-TiO-R-I, C/M = 0.49 \pm 0.04). ¹⁵ However, the bulk of the selections based on optical/NIR CCDs provide an average C/M ratio of 0.68 ± 0.12 , while those based on optical/MIR CCDs provide an average C/M ratio of 0.63 ± 0.04 , and optical/NIR/MIR CCDs give C/M ratios of 0.70 ± 0.08 . The optical and NIR data sets adopted in this investigation cover a significant fraction of the body of the galaxy. Therefore, we decided to investigate the variation of the C/M ratio when using selections based on optical/NIR CCDs. As expected, the population ratios estimated over the entire body of the galaxy are on average 20% smaller than those limited to the innermost cluster regions. The difference is due to the fact that C-rich stars are centrally concentrated, while the O-rich stars cover broader regions and their number steadily increases. This difference takes account of a significant fraction of the differences in the population ratios available in the literature (see Table 6).

We also decided to use the new population ratios to provide a preliminary estimate of the mean metallicity of AGB stars in NGC 6822. Analytical relations correlating the population ratio to the mean iron abundance were provided by Battinelli & Demers (2005) by using a sample of LG galaxies: $[Fe/H] = -1.32(\pm 0.07) - 0.59(\pm 0.09) \times log(C/M)$. The same relation was revised by Cioni (2009), updating metallicity values by using the RGB color method. They found $[Fe/H] = -1.39(\pm 0.06) - 0.47(\pm 0.10) \times log(C/M)$.

We used these relations and the CM ratios listed in Table 5 to estimate mean metallicity for the selected AGB stars, and the new estimated iron abundances are listed in Columns (5) and (6) of the same table. The errors on the iron abundances take account of the uncertainties on both the coefficients of the analytical relations and the CM ratios. The iron abundances listed in Table 5 indicate that AGB stars in NGC 6822 are independent of the adopted calibration and metal intermediate; indeed, we found a mean iron abundance of $[Fe/H] \sim -1.20$ ($\sigma = 0.04$ dex) and $[Fe/H] \sim -1.30$ ($\sigma = 0.03$ dex), respectively. We note that the small values of the standard deviations are a consequence of the mild dependence of the adopted population ratio—metallicity relations on the C/M ratio.

Finally, we compared our results on population ratios and iron abundances with similar estimates available in the literature that are listed in Table 6. C/M ratios are quite different from each other and from our average values, with the exception of the estimate from Hirschauer et al. (2020; 0.599 ± 0.036 , based on NIR/MIR CMDs), which is very similar, within the errors, to our average C/M ratio (0.63 ± 0.04) based on optical/MIR CCDs. On the other side, the mean iron abundances are in good agreement with the literature estimates, except for the value from Kang et al. (2006). Metallicity measurements for NGC 6822 were also obtained by Davidge (2003) by using the slope of the RGB ([Fe/H] = -1 ± 0.3) and from spectroscopic measurements (Venn et al. 2001: [Fe/H] = -0.49 ± 0.22 ; Tolstoy et al. 2001: [Fe/H] = -1 ± 0.5 ; Kirby et al. 2013: [Fe/H] = -1.05 ± 0.01).

^a Battinelli & Demers (2005)

^b Cioni (2009).

 $[\]overline{^{15}}$ Note that in the estimate of the C/M ratio we did not include a sample of 69 fainter/bluer carbon stars, as identified by L02 (see Section 5.2). They deserve a more detailed spectroscopic analysis.

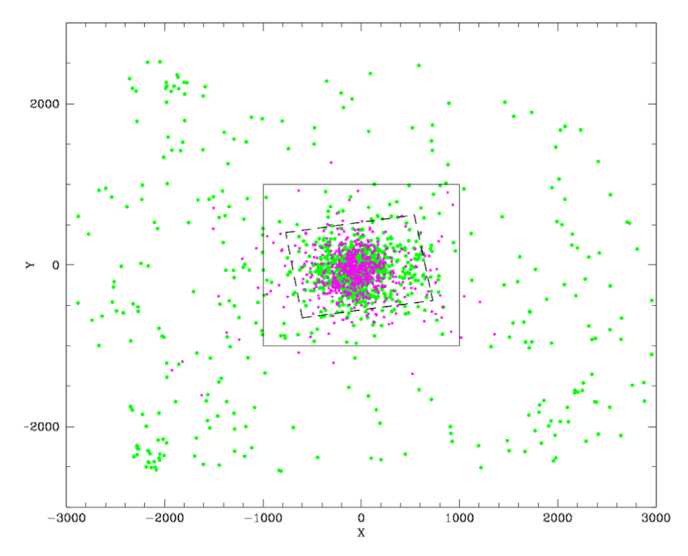


Figure 18. Radial distribution of the C- (magenta circles) and O-rich (green circles) samples selected from the r-K-r-i CCD. The black dashed rectangle delimits the FOV of the Spitzer Space Telescope; the black box of $1000 \, \mathrm{arcsec}^2$ outlines the area within which the star counts were made. Note that most of the C- and O-rich stars are located in a galaxy region entirely covered by the Spitzer data set.

Our estimates agree quite well with spectroscopic measurements of old stellar populations.

7. Summary and Final Remarks

We performed a detailed optical photometric analysis of the nearby dIrr galaxy NGC 6822. We carried out PSF photometry of a large set of g- (61), r- (18), and i-band (27) images collected with the wide-field imager HSC available at the Subaru Telescope. The individual images have an FOV of 1°.5 in diameter, and they include 104 CCDs. The data set includes both shallow ($t \sim 30$ s) and deep ($t \sim 240-300$ s) exposures collected in very good seeing conditions (≤ 0.9 for 50% of the images). These images were complemented with 13 g, r, i images collected with the wide-field imager MegaPrime available at CFHT, with two dozen g, r, i images collected with DECAM available at the CTIO 4 m Blanco telescope and with six g-band images acquired with the WFC available at INT. These data cover the same sky area covered by the Subaru data set, and they have exposure times ranging from 15 to 600 s and seeing similar to the HSC images. The individual images cover an FOV of $1 \times 1 \text{ deg}^2$ (MegaPrime), of 2°.2 in diameter (DECAM), and of $34' \times 34'$ (WFC), and they were included to improve the absolute photometric calibration and the sampling of bright stars. All in all, the current photometric data set covers an area of 2 deg² across the galaxy center with three different photometric bands. We performed PSF photometry over 7115 individual CCD images by using the suites of codes DAOPHOT-ALLSTAR-ALLFRAME. The final catalog includes more than 1 million stars with at least one measurement in two different photometric bands. The maximum number of measurements per star ranges from 74 (g) to 28 (r) to 42 (i). In total, in the three photometric bands we performed 4×10^7 photometric measurements of objects across the entire FOV. The current catalog is the widest and most homogeneous photometric data set ever collected for a nearby dIrr, except for the MCs. The limiting magnitudes range from 14 to 25.8 mag ($\sigma = 0.04$ mag) in the g band (the deepest),

C/M	(Fe/H)	References
1.0 ± 0.2		[1]
0.27 ± 0.03	-0.99 ± 0.02	[2]
~1.05	-1.3 ± 0.2	[3]
0.48 ± 0.02^{a}	-1.24 ± 0.07^{a}	[4]
0.29 ± 0.01^{b}	-1.14 ± 0.08^{b}	[4]
0.95 ± 0.04	-1.38 ± 0.06 [5]	
0.599 ± 0.036	-1.286 ± 0.095	[6]

Notes.

References. [1] L02; [2] Kang et al. (2006); [3] K12; [4] (S12); [5] (S12); [6] Hirschauer et al. (2020).

from 13.7 to 25.5 mag ($\sigma = 0.05$ mag) in the r band, and from 13 to 24.9 mag ($\sigma = 0.09$ mag) in the i band (the shallowest).

To provide a detailed analysis of stellar populations across the entire FOV of the current data set, we developed a new approach to identify candidate field and galaxy stars. We took advantage of the three different photometric bands, and the new algorithm is an iterative procedure based on the 3D CCM diagram. We identified a training set of candidate galaxy stars located at a few arcminutes from the galaxy center, and the key evolutionary sequences were subtracted from the global 3D CCM diagram. After two iterations, we ended up with a catalog of candidate galaxy stars including more than 550,000 stars with at least one measurement in two different photometric bands

Finally, the global optical photometric catalog was cross-correlated with the NIR (S12) and MIR (Khan et al. 2015; Marocco et al. 2021) catalogs available in the literature. The NIR catalog includes JHK photometry, and it is based on the UKIRT images covering almost the same sky area as our optical data set, while the MIR catalogs include both the IRAC photometry from images collected with Spitzer and covering the innermost regions of the galaxy and the CatWISE and AllWISE photometry obtained from the WISE survey and covering an area of $3^{\circ} \times 3^{\circ}$ across the center of galaxy. The global optical–NIR–MIR catalog includes more than 65,000 stars with at least two measurements in optical, NIR, and MIR photometric bands.

The global optical–NIR–MIR catalog has been the stepping stone for several interesting results concerning the stellar content of NGC 6822.

(i) We estimated apparent and absolute total magnitudes in the nine photometric bands adopted in the current investigations. The absolute magnitude ranges from ~ -15 to -16 mag in the three optical (g, r, i) bands, from ~ -15.5 to -16.5 mag in the three NIR (J, H, K) bands, and from ~ -17.6 to -19.3 mag in the three MIR (W1, W2, W3) bands. We also compared the current estimates with the absolute magnitudes of the MCs, which were estimated from the Gaia eDR3 catalog, suggesting that NGC 6822 is fainter in the optical regime than the MCs. However, optical–MIR colors suggest that NGC 6822 is systematically redder than MCs. The difference is mainly caused by the high number of C-rich stars identified in the former system. Furthermore, we found that NGC 6822 in the

 $^{^{\}rm a}$ C/M ratio and metallicity estimated over an area of 4 kpc across the center of NGC 6822.

^b C/M ratio and metallicity estimated over the entire observed area.

MIR CCD (W1 – W2, W2 – W3; Hainline et al. 2016) is located in the blue tail of the so-called "composite" stellar systems (Baldwin et al. 1981; Kewley et al. 2001; Kauffmann et al. 2003), i.e., dwarf galaxies in which the emission-line flux includes contributions from both AGN and star formation activity, thus suggesting that this diagnostic is also prone to possible systematics introduced by AGB stars.

(ii) We performed a new and independent estimate of the center of the galaxy by using two different approaches: 3D histogram and maximum likelihood. The 3D histogram method was applied to the old stellar tracers, and we found that the coordinates of the galaxy center are R.A.(J2000) = $19^{h}44^{m}58^{s}.56$, decl.(J2000) = $-14^{d}47^{m}34^{s}.8$. We also used the maximum likelihood algorithm from Martin et al. (2008) to estimate structural parameters, and the coordinates of the galaxy center agree, within the errors, with the 3D histogram. The difference with previous estimates available in the literature is of the order of 1/15 in R.A. and 1/53 in decl. The spatial distribution and the isocontours of the whole catalog show that the galaxy is almost spherically and symmetrically distributed and includes stars at radial distances larger than 1°. This evidence indicates that the truncation radius of this galaxy is well beyond the current estimates. Moreover, the solution of the fit provided a position angle of $\theta \sim 75^{\circ}$ and a very modest eccentricity ($\epsilon \sim 0.15$) that are in quite fair agreement with similar estimates available in the literature (Battinelli et al. 2006; Zhang et al. 2021).

(iii) The reduction strategy we devised provided deep and accurate CMDs. The i, g-i CMD of candidate galaxy stars (Figure 9) covers more than nine *i*-band magnitudes. This CMD shows several well-defined evolutionary sequences (YMS, RSG, RGB, RC, AGB) suggesting the presence of young, intermediate-age, and old stellar populations in the galaxy. We selected the different stellar tracers on the optical CMD, and in order to overcome possible systematics due to the differential reddening affecting this galaxy, we validated our selections by using the Wesenheit index and by taking advantage of both NIR and MIR photometry. Special attention was paid to the identification of AGB stars. We adopted the same approaches suggested in the literature (L02; Kang et al. 2006) and investigated new optical-NIR-MIR color combinations to further improve the identification and characterization of C- and O-rich stars. We found that the CN-TiO, R-I CCD (defined by L02) and a series of new optical-NIR, optical-MIR, and optical-NIR-MIR CCDs are very solid diagnostics to identify both C- and O-rich stars. The former one was already known in the literature, but the region covered by M-type stars is affected by field-star contamination. The latter ones are very promising because C- and O-rich stars are distributed along either two almost parallel sequences or two sequences with different slopes. In passing, we also note that the optical-NIR r-K-r-i and i-K-r-i CCDs display a separation in two parallel sequences of candidate O-rich stars, suggesting that they might include a younger (bluer sequence) and an older (redder sequence) AGB component. We compared the slopes of the sequences defined by candidate C- and O-rich stars in the different CCDs with the slopes of the respective reddening vectors, finding that they all differ from each other. This means that the dispersion in color present in the adopted CCDs is an intrinsic feature of AGB stars and is minimally affected by differential reddening. Moreover, the current identifications of C- and O-rich samples are fully supported by the positions of the spectroscopically confirmed C- and M-type stars provided by K12 and S12.

(iv) We investigated the radial distributions and provided the structural parameters for the different stellar tracers selected in the optical CMD. The results show that young stellar tracers (MS+RSG) are distributed along a well-defined bar that is offcenter by 0'.46 in R.A. and 1'.26 in decl.; they have a modest half-light radius ($R_{half} \sim 6.3$), and the young stars located outside the bar suggest the possible presence of a disk ($\theta \sim$ -29°). Indeed, their isocontours seems to follow very well the isocontours traced by the HI column density map (de Blok & Walter 2000, 2003, 2006). The intermediate-age stellar tracers (RC) display isodensity contours that are far from being symmetric; they are distributed over a significant fraction of the body of the galaxy ($R_{half} = 11.8$) and have a smaller eccentricity when compared with young stellar tracers ($\epsilon \sim 0.2$ vs. 0.4). The structural properties of the two selected old stellar tracers, TRGB and RGB2 stars, differ from each other. The TRGB stars show an almost spherical distribution $(\epsilon \sim 0.1)$, are almost edge-on with the semimajor axis along the E-W direction and the minor axis along the N-S direction $(\theta \sim 82^{\circ})$, and have the largest half-light radius among the other stellar populations ($R_{\rm half} \sim 14''$). On the other hand, the RGB2 stars display properties that are similar to both TRGB and RC stellar tracers ($\epsilon \sim 0.1$, $\theta \sim 71^{\circ}$, and $R_{half} \sim 10'$.). Moreover, we also found that O- and C-rich stars (AGB) have different properties. The O-rich stars have structural parameters very similar to those of the old tracers ($\epsilon \sim 0.1$, $\theta \sim 89^{\circ}$, and $R_{\text{half}} = 12.4$), thus indicating that they are dominated by oldand intermediate-age progenitors. On the contrary, the C-rich stars are more centrally concentrated and have structural parameters similar to both young (indeed, the peak of the distribution is off-center and $R_{half} = 4.9$) and old stellar tracers ($\epsilon \sim 0.1$).

(v) We estimated the C/M population ratios based on the star counts performed on the selected CCDs, obtaining on average a C/M ratio of 0.68 ± 0.12 for optical/NIR CCDs, a C/M of 0.63 ± 0.04 for optical/MIR CCDs, a C/M of 0.70 ± 0.08 for optical/NIR/MIR CCDs, and a C/M of 0.49 ± 0.04 for the narrow- and broadband photometry (CN–TiO–R–I) CCD. We also provided an estimate of the mean metallicity of AGB stars by using the current C/M population ratios and the empirical relations provided by Battinelli & Demers (2005) and Cioni (2009). We found mean iron abundances of [Fe/H] \sim –1.20 (σ = 0.04 dex) and [Fe/H] \sim –1.30 (σ = 0.03 dex), respectively. Mean metallicity values are in fair agreement with the literature estimates (e.g., K12; S12; Hirschauer et al. 2020; Davidge 2003; Tolstoy et al. 2001), suggesting a metal-intermediate iron abundance.

The approach developed in the current investigation and the definition of new photometric diagnostics to investigate evolutionary properties of stellar populations in nearby stellar systems are a good viaticum for future optical–NIR–MIR photometric surveys. In this context the incoming optical survey by the Vera Rubin Observatory is going to play a key role, since the main survey plans to cover the entire southern sky every three nights in six different photometric bands (u, g, r, i, z, y) with limiting magnitudes (\sim 27–28 mag) that will allow us a complete census of stellar populations older than 10 Gyr (MS turnoff) over the entire LG.

We are grateful to an anonymous referee for her/his positive words concerning the content and the cut of an early version of the current paper, and for her/his very pertinent suggestions that improved its readability.

It is a real pleasure to thank P. Battinelli and S. Demers for sending us their catalog of NGC 6822 in electronic form. We are also very grateful to W. J. G. de Blok for supplying his H I map for NGC 6822 in electronic form.

M. Monelli acknowledges financial support from the Spanish Ministry of Science and Innovation (MICINN) through the Spanish State Research Agency, under the grant PID2020-118778GB-I00 and under the Severo Ochoa Programe 2020-2023 (CEX2019-000920-S). M. Marengo and J.P.M. are supported by the National Science Foundation under grant No. AST-1714534. M.S. acknowledges support from the Science and Technology Facilities Council Consolidated Grant ST/V00087X/1.

This research has made use of the GaiaPortal catalogs access tool, ASI—Space Science Data Center, Rome, Italy (http://gaiaportal.ssdc.asi.it).

This paper is based on data collected at the Subaru Telescope and retrieved from the HSC data archive system, which is operated by the Subaru Telescope and Astronomy Data Center at NAOJ. Data analysis was in part carried out with the cooperation of Center for Computational Astrophysics (CfCA), NAOJ. The HSC collaboration includes the astronomical communities of Japan and Taiwan and Princeton University. The HSC instrumentation and software were developed by the National Astronomical Observatory of Japan (NAOJ), the Kavli Institute for the Physics and Mathematics of the Universe (Kavli IPMU), the University of Tokyo, the High Energy Accelerator Research Organization (KEK), the Academia Sinica Institute for Astronomy and Astrophysics in Taiwan (ASIAA), and Princeton University. Funding was contributed by the FIRST program from the Japanese Cabinet Office, the Ministry of Education, Culture, Sports, Science and Technology (MEXT), the Japan Society for the Promotion of Science (JSPS), Japan Science and Technology Agency (JST), the Toray Science Foundation, NAOJ, Kavli IPMU, KEK, ASIAA, and Princeton University.

The Pan-STARRS1 Surveys (PS1) and the PS1 public science archive have been made possible through contributions by the Institute for Astronomy, the University of Hawaii, the Pan-STARRS Project Office, the Max Planck Society and its participating institutes, the Max Planck Institute for Astronomy, Heidelberg, and the Max Planck Institute for Extraterrestrial Physics, Garching, Johns Hopkins University, Durham University, the University of Edinburgh, the Queens University Belfast, the Harvard-Smithsonian Center for Astrophysics, the Las Cumbres Observatory Global Telescope Network Incorporated, the National Central University of Taiwan, the Space Telescope Science Institute, the National Aeronautics and Space Administration under grant No. NNX08AR22G issued through the Planetary Science Division of the NASA Science Mission Directorate, the National Science Foundation grant No. AST-1238877, the University of Maryland, Eotvos Lorand University (ELTE), the Los Alamos National Laboratory, and the Gordon and Betty Moore Foundation.

This work is based in part on observations made with the Spitzer Space Telescope, which is operated by the Jet Propulsion Laboratory, California Institute of Technology,

under a contract with the National Aeronautics and Space Administration (NASA).

Some of the data reported here were obtained as part of the UKIRT Service Programme. UKIRT is owned by the University of Hawaii (UH) and operated by the UH Institute for Astronomy. When some of the data reported here were obtained, UKIRT was operated by the Joint Astronomy Centre on behalf of the Science and Technology Facilities Council of the U.K.

This publication makes use of data products from the Widefield Infrared Survey Explorer, which is a joint project of the University of California, Los Angeles, and the Jet Propulsion Laboratory/California Institute of Technology, funded by the National Aeronautics and Space Administration.

This publication makes use in part of data products from the Two Micron All Sky Survey, which is a joint project of the University of Massachusetts and the Infrared Processing and Analysis Center/California Institute of Technology, funded by the National Aeronautics and Space Administration and the National Science Foundation.

This work presents results from the European Space Agency (ESA) space mission Gaia. Gaia data are being processed by the Gaia Data Processing and Analysis Consortium (DPAC). Funding for the DPAC is provided by national institutions, in particular the institutions participating in the Gaia MultiLateral Agreement (MLA).

We made use of the VizieR catalog access tool, provided by CDS, Strasbourg, France (DOI: 10.26093/cds/vizier).

Software: Astropy (Astropy Collaboration et al. 2013), Numpy (Harris et al. 2020), SExtractor (Bertin & Arnouts 1996), Topcat (Taylor 2005).

Appendix A Identification of the Peak Associated with RC Stars

We already mentioned in Section 5.1 that RC stars are solid tracers of intermediate-age stellar tracers. However, the identification of the peak associated with RC stars is far from being trivial, in a stellar system like NGC 6822, because the magnitudes and colors of RC stars in optical CMDs overlap with RGB stars. To overcome this limitation, we adopted the same approach suggested by Sanna et al. (2008) for investigating stellar populations in IC 10. Figure 19 shows the 3D histogram of a i, g - i CMD. The CMD was split with a grid in magnitude and color, and the Z-axis shows the number of stars per grid point. The number of stars was smoothed with a Gaussian kernel with a unitary weight and σ equal to the Poisson error associated with the star count. We performed a series of test and trials to properly identify the optimal bin size in magnitude and in color, and Figure 19 shows the final outcome. Data plotted in this figure display, from left to right, several well-defined, but relatively shallow, evolutionary sequences, namely, the YMS, the RSG, and the AGB stars. The steady increase in star counts located in the central region of the CMD is associated, from top to bottom, with TRGB and RGB stars. A preliminary comparison with evolutionary models suggests that the main peak located at $i \sim 24$ mag and $g - i \sim 1$ mag is caused by RC stars. A more detailed discussion concerning the comparison between theory and observations will be addressed in a forthcoming paper (M. Tantalo et al. 2022, in preparation).

To constrain on a more quantitative basis the location of RC stars, we isolated the star counts associated with RG stars and

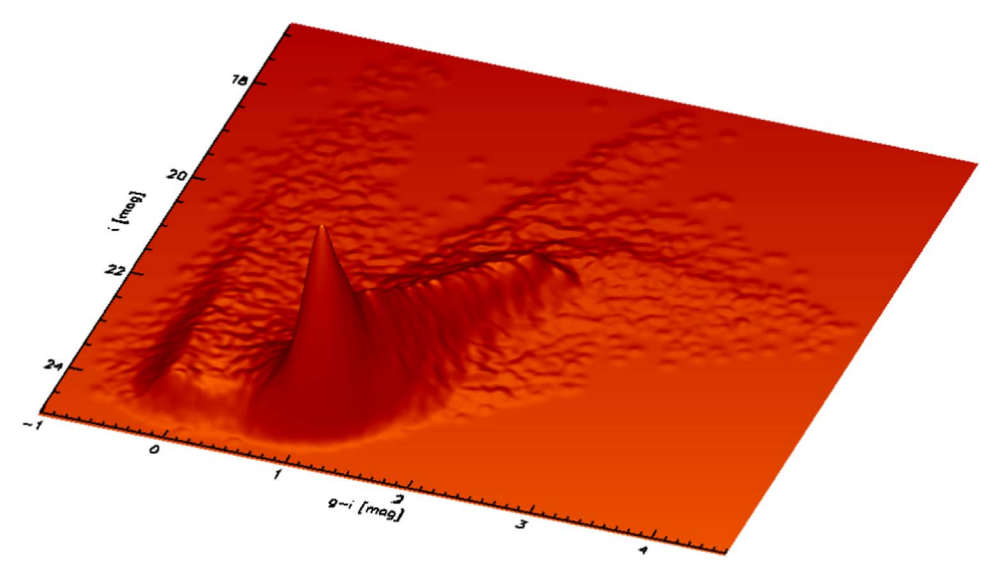


Figure 19. 3D histogram of the i, g - i CMD. The view is from the faint to the brighter limit of the CMD. Note that in this CMD we are plotting all the stars with at least one measurement in g and i bands. The Z-axis is in arbitrary units. From bluer to redder colors the relatively shallow sequences are associated with YMS, RSG, and AGB stars. The steady increase in the star counts present in the central regions is associated with RG stars. The main peak is associated with RC stars.

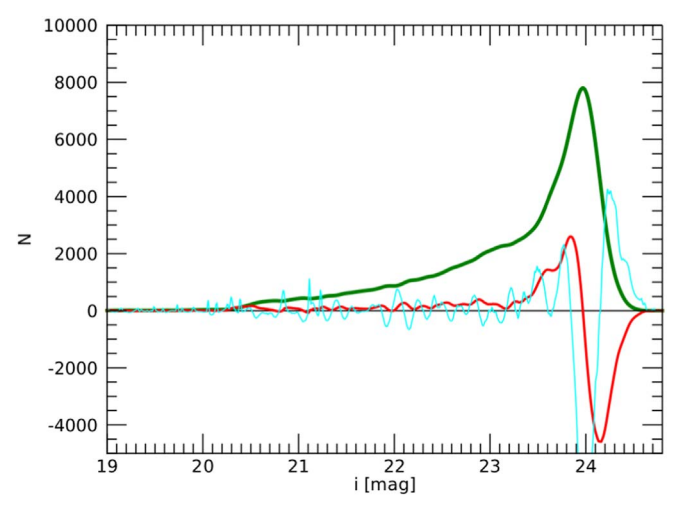


Figure 20. Ridge line in magnitude (*i* band; green line) of the star counts associated with RG stars shown in Figure 19. The red and cyan lines show, respectively, the first and second derivatives of the ridge line.

estimated the ridge line in magnitude. Figure 20 shows the ridge line in magnitude (green line) and its first and second derivatives (red and cyan lines). The maximum in the ridge line and the minimum in the first derivative located at $i \sim 23.9-24.0$ mag trace the RC stars.

Appendix B Selection of Candidate Galaxy Stars for the Magellanic Clouds

The selections for the MCs were obtained by querying the Gaia eDR3 database. In particular, we selected a sky area with a 20° radius around the center of the LMC and with a sky area

with 11° radius for the SMC by using the following selection criteria to control the quality of the data: not duplicated_source; with color bp_rp measured; with astrometric solutions with either five or six parameters; not QSO; ruwe < 1.4; G < 20.5; C < 1.0. The C is the corrected phot_bp_rp_excess_factor introduced by Riello et al. (2021), which helps to remove background galaxies; bright QSOs can be identified by using the agn_cross_id table included in the Gaia release.

We ended up with a sample including 4,134,870 objects for the SMC and 14,716,026 objects for the LMC (see the top left panels of Figures 21 and 22). The exquisite quality of Gaia astrometric data allowed us to separate the stellar populations of the MCs from the foreground field stars by using the propermotion selection criteria. To determine the mean proper motion of both the LMC and SMC, we used subsamples of objects that are closer than 0.5° to the centers of the galaxies and then computed a Gaussian fit of the individual μ_{α^*} and μ_{δ} distributions. Therefore, we obtained the centers of proper motion at [0.68, -1.23] mas yr⁻¹ for the SMC and [1.89,0.36] mas yr⁻¹ for the LMC. Subsequently, we selected all the objects compatible, within 10 times the errors, with the quoted mean proper motions (see the top right panel of Figures 21 and 22). Finally, we minimized the foreground contamination by selecting stars with parallax/parallax_{error} < 5. This parallax cut excludes solutions that are not compatible with being distant enough to be part of the LMC or SMC, and therefore possible foreground contamination from MW stars. The final samples include 2,380,151 stars for the SMC and 12,456,270 stars for the LMC (see the middle panels of Figures 21 and 22). We also took advantage of the precomputed cross-matches of the Gaia catalog with visual and infrared large surveys (Marrese et al. 2019), in particular, with 2MASS (see the bottom panels of Figures 21 and 22), to further constrain the properties of candidate galaxy stars.

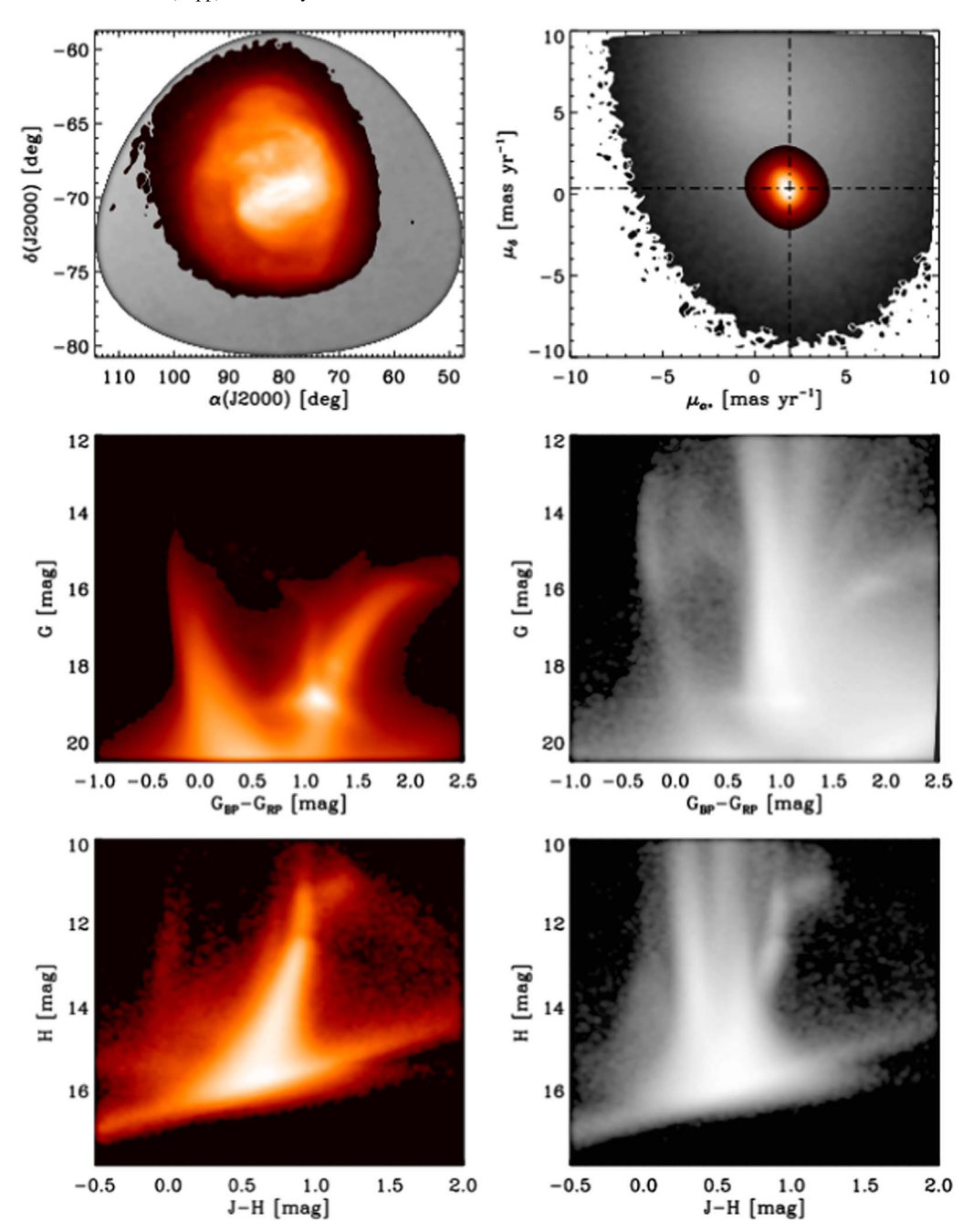


Figure 21. Top: sky coverage (left) and proper motions (right) of the candidate LMC stars (colored). The gray region highlights candidate field stars. Middle: optical, G, $G_{\rm BP}-G_{\rm RP}$, CMD for candidate LMC (left) and field (right) stars. Bottom: same as the middle panels, but for the NIR, H, J-H, CMD.

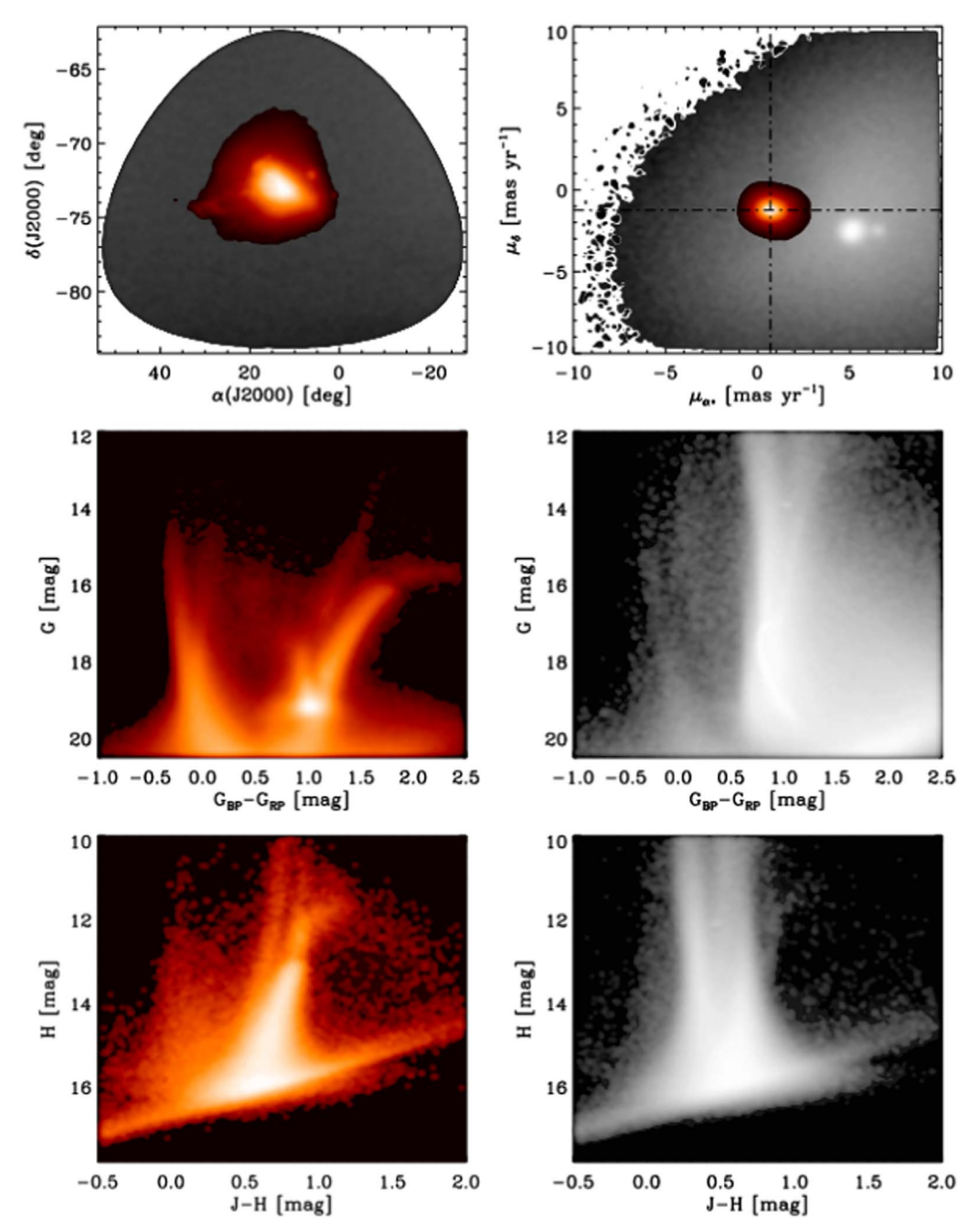


Figure 22. Same as Figure 21, but for candidate SMC and field stars.

ORCID iDs

Maria Tantalo https://orcid.org/0000-0002-6829-6704
Massimo Dall'Ora https://orcid.org/0000-0001-8209-0449
Giuseppe Bono https://orcid.org/0000-0002-4896-8841
Peter B. Stetson https://orcid.org/0000-0001-6074-6830
Michele Fabrizio https://orcid.org/0000-0001-5829-111X
Mario Nonino https://orcid.org/0000-0001-5829-111X
Mario Nonino https://orcid.org/0000-0001-7511-2830
Giuliana Fiorentino https://orcid.org/0000-0001-7511-2830
Giuliana Fiorentino https://orcid.org/0000-0003-0376-6928
Massimo Marengo https://orcid.org/0000-0001-9910-9230
Matteo Monelli https://orcid.org/0000-0001-5292-6380
Joseph P. Mullen https://orcid.org/0000-0002-1650-2764
Adriano Pietrinfemi https://orcid.org/0000-0003-3795-9031
Maurizio Salaris https://orcid.org/0000-0002-2744-1928

Astropy Collaboration, Robitaille, T. P., Tollerud, E. J., et al. 2013, A&A, 558, A33

Baldacci, L., Rizzi, L., Clementini, G., & Held, E. V. 2005, A&A, 431, 1189

Baldwin, J. A., Phillips, M. M., & Terlevich, R. 1981, PASP, 93, 5

Battinelli, P., & Demers, S. 2005, A&A, 434, 657

Battinelli, P., & Demers, S. 2011, A&A, 525, A69

Battinelli, P., Demers, S., & Kunkel, W. E. 2006, A&A, 451, 99

Bertin, E., & Arnouts, S. 1996, A&AS, 117, 393

Boyer, M. L., McDonald, I., Srinivasan, S., et al. 2015, ApJ, 810, 116

Boyer, M. L., Srinivasan, S., van Loon, J. T., et al. 2011, AJ, 142, 103

Bono, G., Iannicola, G., Braga, V. F., et al. 2019, ApJ, 870, 115

Bono, G., Stetson, P. B., Sanna, N., et al. 2008, ApJL, 686, L87

Bono, G., Stetson, P. B., VandenBerg, D. A., et al. 2010a, ApJL, 708, L74

Bono, G., Stetson, P. B., Walker, A. R., et al. 2010b, PASP, 122, 651

Calamida, A., Zocchi, A., Bono, G., et al. 2020, ApJ, 891, 167

References

```
Cannon, J. M., O'Leary, E. M., Weisz, D. R., et al. 2012, ApJ, 747, 122
Cannon, J. M., Walter, F., Armus, L., et al. 2006, ApJ, 652, 1170
Cardelli, J. A., Clayton, G. C., & Mathis, J. S. 1989, ApJ, 345, 245
Castellani, V., Cignoni, M., Degl'Innocenti, S., et al. 2002, MNRAS, 334, 69
Cioni, M.-R. L. 2009, A&A, 506, 1137
Clementini, G., Held, E. V., Baldacci, L., & Rizzi, L. 2003, ApJL, 588, L85
Cutri, R. M., Wright, E. L., Conrow, T., et al. 2013, Explanatory Supplement to
   the AllWISE Data Release Products, https://wise2.ipac.caltech.edu/docs/
   release/allwise/expsup/index.html
Dale, D. A., Gil de Paz, A., Gordon, K. D., et al. 2007, ApJ, 655, 863
Davidge, T. J. 2003, PASP, 115, 635
Davidge, T. J. 2005, AJ, 130, 2087
de Blok, W. J. G., & Walter, F. 2000, ApJL, 537, L95
de Blok, W. J. G., & Walter, F. 2003, MNRAS, 341, L39
de Blok, W. J. G., & Walter, F. 2006, AJ, 131, 343
Du, X., Shapley, A. E., Tang, M., et al. 2020, ApJ, 890, 65
Feast, M. W., Whitelock, P. A., Menzies, J. W., & Matsunaga, N. 2012,
         AS, 421, 2998
Fusco, F., Buonanno, R., Bono, G., et al. 2012, A&A, 548, A129
Fusco, F., Buonanno, R., Hidalgo, S. L., et al. 2014, A&A, 572, A26
Gallart, C., Aparicio, A., & Vilchez, J. M. 1996, AJ, 112, 1928
Gallouet, L., Heidmann, N., & Dampierre, F. 1975, A&AS, 19, 1
Gieren, W., Pietrzyński, G., Nalewajko, K., et al. 2006, ApJ, 647, 1056
Girardi, L., Barbieri, M., Groenewegen, M. A. T., et al. 2012, Red Giants as
  Probes of the Structure and Evolution of the Milky Way (Berlin:
   Springer), 165
Gottesman, S. T., & Weliachew, L. 1977, A&A, 61, 523
Graczyk, D., Pietrzyński, G., Thompson, I. B., et al. 2020, ApJ, 904, 13
Hainline, K. N., Reines, A. E., Greene, J. E., et al. 2016, ApJ, 832, 119
Harris, C. R., Millman, K. J., van der Walt, S. J., et al. 2020, Natur, 585, 357
Hirschauer, A. S., Gray, L., Meixner, M., et al. 2020, ApJ, 892, 91
Hodge, P., Smith, T., Eskridge, P., et al. 1991, ApJ, 379, 621
Hubble, E. P. 1925, ApJ, 62, 409
Huxor, A. P., Ferguson, A. M. N., Veljanoski, J., et al. 2013, MNRAS,
   429, 1039
Hwang, N., Lee, M. G., Lee, J. C., et al. 2011, ApJ, 738, 58
Joshi, Y. C., & Panchal, A. 2019, A&A, 628, A51
Kacharov, N., Rejkuba, M., & Cioni, M.-R. L. 2012, A&A, 537, A108
Kang, A., Sohn, Y.-J., Kim, H.-I., et al. 2006, A&A, 454, 717
Kauffmann, G., Heckman, T. M., Tremonti, C., et al. 2003, MNRAS,
   346, 1055
Kennicutt, R. C., Armus, L., Bendo, G., et al. 2003, PASP, 115, 928
Kewley, L. J., Dopita, M. A., Sutherland, R. S., et al. 2001, ApJ, 556, 121
Khan, R., Stanek, K. Z., Kochanek, C. S., & Sonneborn, G. 2015, ApJS,
  219, 42
Kinson, D. A., Oliveira, J. M., & van Loon, J. T. 2021, MNRAS, 507, 5106
Kirby, E. N., Cohen, J. G., Guhathakurta, P., et al. 2013, ApJ, 779, 102
Larsen, S. S., Brodie, J. P., Wasserman, A., & Strader, J. 2018, A&A, 613, A56
Lee, M. G., Freedman, W. L., & Madore, B. F. 1993, ApJ, 417, 553
Lee, H., Skillman, E. D., & Venn, K. A. 2006, ApJ, 642, 813
```

```
Letarte, B., Demers, S., Battinelli, P., & Kunkel, W. E. 2002, AJ, 123, 832
Madore, B. E. 1976, MNRAS, 177, 157
Madore, B. F., Rigby, J., Freedman, W. L., et al. 2009, ApJ, 693, 936
Marocco, F., Eisenhardt, P. R. M., Fowler, J. W., et al. 2021, ApJS, 253, 8
Marrese, P. M., Marinoni, S., Fabrizio, M., et al. 2019, A&A, 621, A144
Martin, N. F., de Jong, J. T. A., & Rix, H.-W. 2008, ApJ, 684, 1075
Martínez-Vázquez, C. E., Stetson, P. B., Monelli, M., et al. 2016, MNRAS,
  462, 4349
Massey, P., Armandroff, T. E., Pyke, R., et al. 1995, AJ, 110, 2715
Mateo, M. L. 1998, ARA&A, 36, 435
McConnachie, A. W. 2012, AJ, 144, 4
Mennickent, R. E., Gieren, W., Soszyński, I., & Pietrzyński, G. 2006, A&A,
  450, 873
Neugent, K., & Massey, P. 2019, Galax, 7, 74
Papovich, C., Shipley, H. V., Mehrtens, N., et al. 2016, ApJS, 224, 28
Parada, J., Heyl, J., Richer, H., Ripoche, P., & Rousseau-Nepton, L. 2021,
         AS, 501, 933
Patrick, L. R., Evans, C. J., Davies, B., et al. 2015, ApJ, 803, 14
Pietrzyński, G., Gieren, W., Udalski, A., et al. 2004, AJ, 128, 2815
Pietrzyński, G., Graczyk, D., Gallenne, A., et al. 2019, Natur, 567, 200
Reines, A. E. 2022, NatAs, 6, 26
Renzini, A., & Buzzoni, A. 1986, in Spectral Evolution of Galaxies: Proc. of
  the Fourth Workshop (Dordrecht: Reidel), 195
Rich, J. A., Persson, S. E., Freedman, W. L., et al. 2014, ApJ, 794, 107
Riello, M., De Angeli, F., Evans, D. W., et al. 2021, A&A, 649, A3
Robin, A. C., Reylé, C., Fliri, J., et al. 2014, A&A, 569, A13
Sanna, N., Bono, G., Stetson, P. B., et al. 2008, ApJL, 688, L69
Schlegel, D. J., Finkbeiner, D. P., & Davis, M. 1998, ApJ, 500, 525
Shapley, H. 1923, BHarO, 796, 1
Sibbons, L. F., Ryan, S. G., Cioni, M.-R. L., et al. 2012, A&A, 540, A135
Sibbons, L. F., Ryan, S. G., Napiwotzki, R., & Thompson, G. P. 2015, A&A,
  574, A102
Stetson, P. B. 1987, PASP, 99, 191
Stetson, P. B. 1994, PASP, 106, 250
Stott, J. P., Sobral, D., Smail, I., et al. 2013, MNRAS, 430, 1158
Sweigart, A. V., Greggio, L., & Renzini, A. 1989, ApJS, 69, 911
Sweigart, A. V., Greggio, L., & Renzini, A. 1990, ApJ, 364, 527
Taylor, M. B. 2005, in ASP Conf. Ser. 347, Astronomical Data Analysis
  Software and Systems XIV, ed. P. L. Shopbell, M. C. Britton, & R. Ebert
  (San Francisco, CA: ASP), 29
Tolstoy, E., Irwin, M. J., Cole, A. A., et al. 2001, MNRAS, 327, 918
Tonry, J. L., Stubbs, C. W., Lykke, K. R., et al. 2012, ApJ, 750, 99
van den Bergh, S. 1968, JRASC, 62, 145
Venn, K. A., Lennon, D. J., Kaufer, A., et al. 2001, ApJ, 547, 765
Warren, S. J., Hambly, N. C., Dye, S., et al. 2007, MNRAS, 375, 213
Weiss, A., & Ferguson, J. W. 2009, A&A, 508, 1343
Whitelock, P. A., Menzies, J. W., Feast, M. W., et al. 2013, MNRAS,
  428, 2216
Wright, E. L., Eisenhardt, P. R. M., Mainzer, A. K., et al. 2010, AJ, 140, 1868
Zhang, S., Mackey, D., & Da Costa, G. S. 2021, MNRAS, 508, 2098
```